Bioactive Materials 50 (2025) 396–413

Contents lists available at ScienceDirect

Bioactive Materials

journal homepage: www.keaipublishing.com/en/journals/bioactive-materials

Pathology-inspired collagen-binding thermosensitive micelle drops enable prolonged and efficient treatment of fungal keratitis

Maoyu Cai [a,b,1], Haiping Zhong [c,f,1], Xindi Wang [a,b,1], Liangpin Li [b], Xueyan Zhou [g], Yan Wang [b,*], Xia Hua [d,e,**], Shutao Guo [c,***], Xiaoyong Yuan [b,****]

[a] Clinical College of Ophthalmology, Tianjin Medical University, Tianjin, 300020, China
[b] Tianjin Key Laboratory of Ophthalmology and Visual Science, Tianjin Eye Institute, Tianjin Eye Hospital, Tianjin, 300020, China
[c] Key Laboratory of Functional Polymer Materials of Ministry of Education, State Key Laboratory of Medicinal Chemical Biology and Institute of Polymer Chemistry, College of Chemistry, Nankai University, Tianjin, 300071, China
[d] Aier Eye Institute, Changsha, 410015, China
[e] Aier Eye Hospital, Tianjin University, Tianjin, 300110, China
[f] School of Biomedical Engineering, Guangzhou Medical University, Guangzhou, 510260, China
[g] School of Medicine, Nankai University, Tianjin, 300071, China

A B S T R A C T

Fungal keratitis (FK) is a challenging-to-manage blinding corneal infectious disease that often leads to severe sequelae, such as corneal leukoplakia regardless of curative care. Moreover, the unique anatomical structure and tear turnover of the eye significantly limit the bioavailability and therapeutic efficacy of traditional eye drops. Inspired by the unique pathological features of corneal ulcers, we report a thermosensitive multifunctional eye drop, designated PX-TA, based on a poloxamer (PX) and a collagen-adhesive tannic acid (TA), for prolonged and efficient treatment of FK. PX-TA transforms into a gel at body temperature and adheres to exposed collagen at the ulcer site; this significantly improves the corneal retention time and bioavailability. PX-TA maintains corneal retention for at least 90 min, substantially exceeding both the 15-min limit of commercial mucoadhesive eye drops and the 30-min threshold of conventional in situ gels. When loaded with amphotericin B (AmB), once-daily PX-TA-AmB administration effectively suppresses inflammation and corneal scarring, demonstrating superior efficacy over six-times-daily free AmB drops and a good safety profile. Mechanistic investigations reveal that PX-TA-AmB mediates its therapeutic effects through the MAPK6/PI3K/AKT signaling pathway. Moreover, the metal-chelating properties of TA inhibit the copper-dependent enzyme lysyl oxidase (LOX), resulting in reduced matrix fibrosis. Overall, the use of PX-TA-AmB drops represents a simplified yet effective strategy for the potential clinical management of FK, inspiring the design of eye drop formulations.

1. Introduction

Fungal keratitis (FK) is also commonly known as fungal corneal ulcer and is one of the most common corneal infections leading to blindness. It is particularly prevalent in agriculture-dominated countries, where the blindness rate exceeds 60 %, even with treatment [1,2]. Its primary symptoms—pain, tearing, photophobia, and vision loss—are closely associated with corneal ulcers, which not only represent the main pathological feature of the disease but also accelerate symptom progression [3,4]. The corneal ulcer pathological cascade is initiated by microbial invasion through compromised epithelial barriers, followed by pathogen-mediated collagenase secretion and inflammatory cell infiltration; this ultimately leads to stromal degradation and characteristic ulcerative crater formation with potential progression to corneal perforation [4,5]. Moreover, corneal ulcers caused by FK are more prone to perforation than those resulting from other infections; this often leads to endophthalmitis and irreversible blindness [6]. Consequently, corneal ulcers have long been recognized as critical warning signs in cases of infectious keratitis, particularly FK [2,5,7,8].

Among the current treatments for FK, eye drops still account for more than 90 % of all ophthalmic formulations [9], despite recent advances in hydrogels, ointments, and contact lenses [10–12]. However,

Peer review under the responsibility of editorial board of Bioactive Materials.
* Corresponding author.
** Corresponding author. Aier Eye Institute, Changsha, 410015, China.
*** Corresponding author.
**** Corresponding author.
E-mail addresses: wangyan7143@vip.sina.com (Y. Wang), cathayhuaxia@163.com (X. Hua), stguo@nankai.edu.cn (S. Guo), yuanxy_cn@hotmail.com (X. Yuan).
[1] These authors contributed equally to this work.

https://doi.org/10.1016/j.bioactmat.2025.04.011
Received 9 January 2025; Received in revised form 29 March 2025; Accepted 11 April 2025

first-line therapies such as amphotericin B (AmB) and natamycin eye drops face significant limitations due to rapid precorneal clearance, which impedes drug retention and leads to low bioavailability [2,13–15]. As a result, frequent dosing, sometimes several times per day during the acute phase, becomes necessary. This, in turn, leads to poor patient compliance, increased hospitalization rates, and the potential development of antifungal resistance [15,16]. Furthermore, systemic antifungal treatments are typically reserved as adjuncts to topical therapy in severe cases because of the blood–ocular barrier and the significant toxic side effects associated with systemic administration [14,15].

To address these therapeutic challenges, various innovative strategies have been developed to overcome rapid precorneal clearance [17–21]. For example, an innovative gold nano-urchins platform can significantly enhance corneal retention through surface engineering, achieving remarkable ~150-fold improvement in retention at 7 days post-instillation compared with smooth-surfaced gold nanoparticles via enhanced cytoadhesion and bioadhesion capabilities [17]. Alginate functionalization has substantially improved precorneal retention via hydrogen bonding interactions and increased viscosity [18]. Microneedle-based strategies have been implemented for corneal drug delivery [21] and enable improved mechanical engagement with corneal tissue by facilitating precise penetration and better adhesion to the corneal surface, thereby extending precorneal retention to 2 h. However, due to the debilitated corneal structure during infection, characterized by epithelial detachment and stromal dissolution, microneedles may induce irreversible corneal damage. Mucoadhesive polymers, which are designed to directly interact with ocular surface mucins, have been utilized in various ophthalmic formulations to noninvasively extend the corneal retention time [22–24]. Nevertheless, the dynamic nature of corneal mucin secretion, coupled with mechanical clearance through blinking and tear turnover, continues to limit retention duration under pathophysiological conditions. These constraints highlight the critical need for delivery systems that optimize both safety and adhesion profiles in infectious keratitis treatment.

Among various ocular drug delivery systems, thermosensitive in situ gels have become effective candidates to address these challenges [25–31]. A key characteristic of these formulations is their reversible gel–phase transition within the physiological temperature range, enabled by the presence of a critical temperature. This approach allows hydrogels to be introduced with minimal invasiveness and provides significant development potential. Various thermosensitive polymers have been explored for their ability to increase corneal retention time. Traditional designs often incorporate excipients such as cellulose derivatives and hyaluronic acid to increase viscosity. However, low-adhesion hydrogels are still rapidly cleared by blinking. Furthermore, excessively enhancing the adhesiveness of hydrogels unavoidably increases their adhesion to nontargeted tissues; this significantly affects ocular comfort and potentially causes adhesion between the eyelid and the eyeball [32].

Guided by pathology-driven drug delivery system design principles [26,33,34], we developed a facile yet efficient multifunctional hydrogel ophthalmic system for FK treatment by exploiting the distinctive pathological features of corneal ulcers (Scheme 1). The design strategy was fundamentally inspired by the unique pathological architecture of corneal ulcers: under physiological conditions, the corneal epithelial barrier prevents external interaction with stromal collagen, which is abundantly distributed throughout the corneal stroma and functions as a target for directional carrier adhesion; during FK progression, ulceration disrupts this protective barrier, and stromal collagen is exposed in a manner analogous to dermal wound formation. Since tannic acid (TA) is enriched with catechol and gallol groups and has strong interactions with collagen through hydrophobic forces and hydrogen bonding networks [35,36], we exploited this pathological modification by

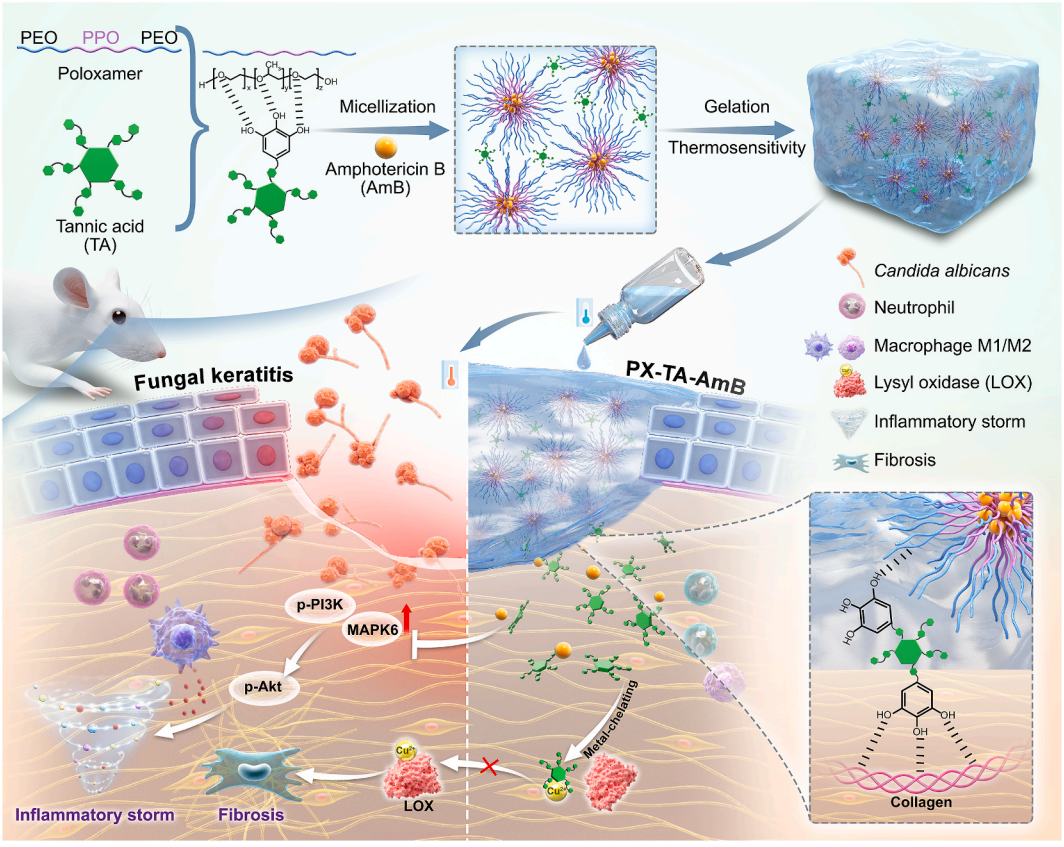

Scheme 1. Schematic illustration of the preparation of PX-TA-AmB eye drops and their collagen binding for the treatment of FK.

incorporating poloxamer (PX), which is a representative thermosensitive polymer, to create a responsive delivery system with multifunctional capabilities. The PX-TA hydrogel undergoes a sol–gel transition at the ulcer site, enabling targeted adhesion to exposed collagen and facilitating localized drug release. Notably, due to this collagen binding mechanism, AmB-loaded PX-TA (PX-TA-AmB) hydrogel eye drops can maintain their position at the ulcer site for at least 90 min post-administration; this time substantially exceeds the 30-min threshold of conventional in situ gel formulations [37–40]. This extended corneal retention directly enhances therapeutic efficacy and amplifies the bioactive properties of TA; thus, compared with the free AmB drops, which need to be administered six times daily as the current clinical therapy, once-daily PX-TA-AmB administration achieves superior therapeutic outcomes. This multifunctional delivery system combines prolonged retention, potent antimicrobial activity, inflammation control, and scar reduction, synergistically improves the therapeutic outcomes, has substantial potential for both FK treatment and clinical translation and can be used to establish a promising paradigm for designing drug delivery systems for the treatment of infectious keratitis, including FK.

2. Results and discussion

2.1. Preparation and characterization of the PX-TA eye drops and AmB loading

To facilitate the preparation of multifunctional collagen-binding hydrogel eye drops, the triblock copolymers PX407 (P407) and PX188 (P188), which consist of poly(ethylene oxide) and poly(propylene oxide) (PEO-PPO-PEO), were employed as hydrogel-forming materials

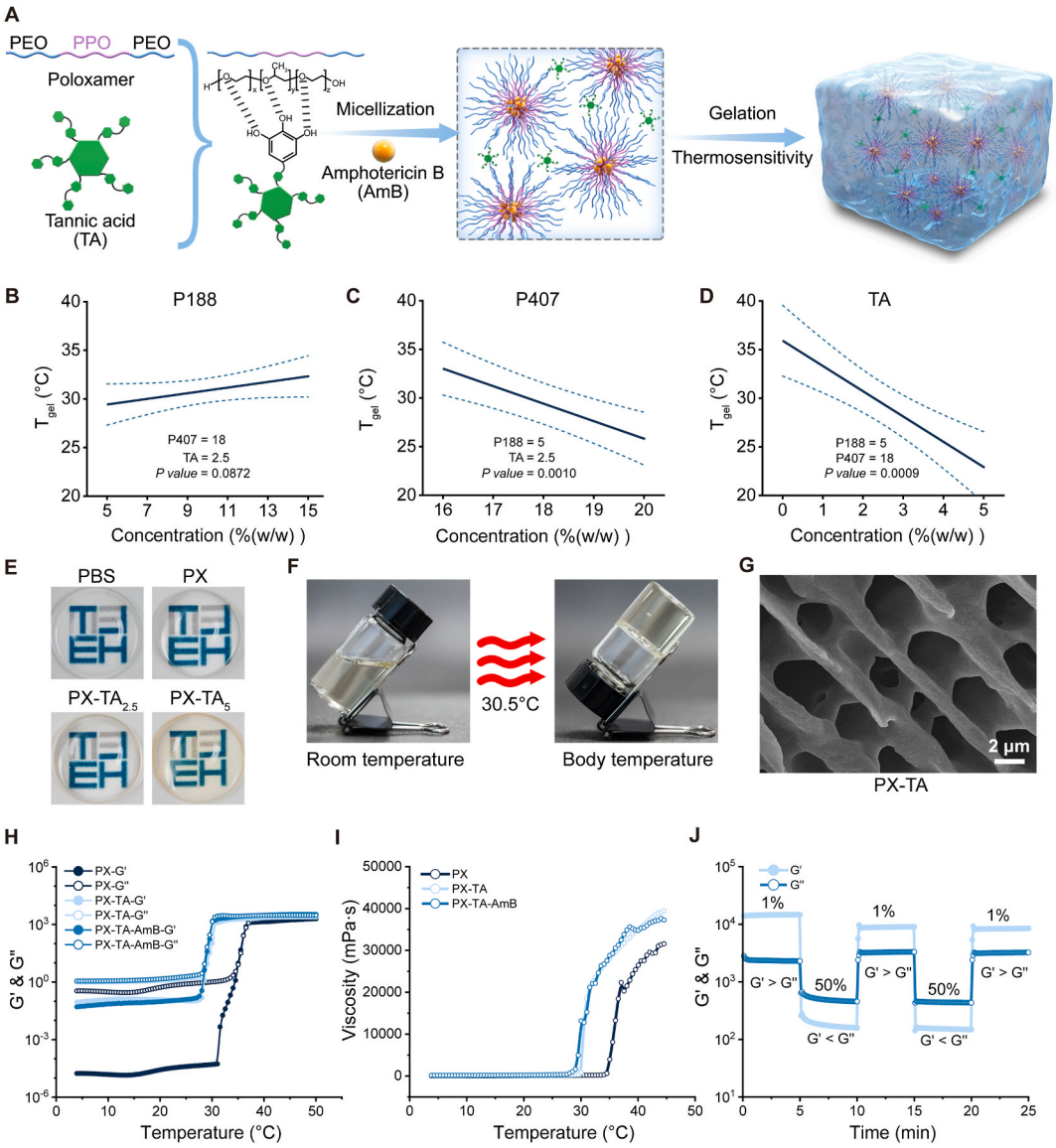

Fig. 1. Preparation and characterization of the PX-TA and PX-TA-AmB eye drops. (A) Schematic representation of the preparation process for the PX-TA and PX-TA-AmB eye drops. (B–D) Structure–property relationships between the concentrations of different eye drop components (P188, P407, TA) and the gel transition temperature (T_{gel}). (E) Transparency observations of PX (containing 18 % P407 and 5 % P188), PX-$TA_{2.5}$ (containing 18 % P407, 5 % P188, and 2.5 % TA), and PX-TA_5 (containing 18 % P407, 5 % P188, and 5 % TA). (F) Actual images of PX-TA (containing 18 % P407, 5 % P188, and 2.5 % TA) at room temperature (24 °C) and the corneal physiological temperature (30.5 °C). (G) SEM image of the PX-TA (containing 18 % P407, 5 % P188, and 2.5 % TA) hydrogel. (H–J) Rheological properties of PX (containing 18 % P407 and 5 % P188), PX-TA (containing 18 % P407, 5 % P188, and 2.5 % TA), and PX-TA-AmB (containing 18 % P407, 5 % P188, 2.5 % TA, and 0.2 % AmB), including (H) rheological behavior at different temperatures, (I) viscosity at different temperatures, and (J) rheological behavior under 1 % and 50 % strain cycles.

(Fig. 1A) because of their excellent and stable thermosensitive sol–gel transitions below 37 °C. PX can form micelles in aqueous solution, and at the gelation temperature, the micelle form is converted to a hydrogel. However, their poor adhesion capacity post-gelation has limited further development of eye drops. Since the cornea undergoes 10–20 blinks per min as delicate transparent tissue, optimal eye drops need to demonstrate sufficient corneal retention to extend the duration of drug efficacy.

TA is a natural adhesive molecule rich in phenolic hydroxyl groups. Based on our previous study [36], we propose that the addition of TA to the PX hydrogel can increase the adhesive ability to bind with collagen, which is exposed under corneal ulcer conditions. PX-TA can be easily fabricated by simply mixing PX and TA in an aqueous solution. ^{1}H nuclear magnetic resonance (NMR) analysis confirmed the presence of both PX and TA proton peaks in PX-TA, and the ratio of TA to PX was consistent with the feed ratio determined by the integration of characteristic peaks; these results indicated that PX and TA were sufficiently connected to form a hydrogel (Fig. S1B). The phenolic hydroxyl groups from TA could form hydrogen bonds with the oxygen in PX. As observed from the FT-IR spectra, the vibration of the carbonyl bond of TA shifted from 1697 to 1730 cm^{-1}; these results indicated that the formation of intermolecular hydrogen bonds between the poloxamer and the hydroxyl group of TA weakened the intramolecular hydrogen bonding between the hydroxyl and carbonyl bonds of TA (Fig. S1A).

While enhancing adhesion, TA significantly reduces the sol–gel transition temperature (T_{gel}). Hydrogels based on TA and P407 exhibit a T_{gel} near or below room temperature, impeding their clinical translation [41]. Due to the unique physiological temperature of the cornea, the ideal T_{gel} for thermosensitive eye drop hydrogel formulations should be between room temperature and the precorneal temperature, with an optimal T_{gel} value of 30 ± 2 °C [42–44]. To optimize T_{gel} for corneal drug delivery, the more hydrophilic P188 was incorporated. To optimize the T_{gel} of the PX-TA hydrogel, a Box–Behnken experimental design was carried out to investigate the influence of PX and TA on T_{gel}; here, P188 (w/v), P407 (w/v), and TA (w/v) concentrations were used as independent variables, and T_{gel} was used as the dependent variable. As shown by ANOVA (Table S1) and the relationships between T_{gel} and P188 (Fig. 1B), P407 (Fig. 1C), and TA (Fig. 1D), the hydrogel T_{gel} was significantly negatively correlated with the P407 and TA concentrations ($p < 0.05$). Ocular formulations needed to maintain maximum transparency to ensure visual quality. We found that all the PX-TA hydrogels were transparent even with 5 % TA (w/v) and presented notable light-yellow coloration (Fig. 1E). This opacity originated from the inherent dark yellow nature of TA and compromised hydrogel transparency at high concentrations. Such color change may impose some limitations on clinical translation, including vision blurring or color distortion, interference with certain ophthalmic examinations (such as fundus examination and fluorescein sodium staining tests), and causing patient concerns about medication quality (as the unusual color might be misinterpreted as contamination or degradation). Furthermore, high TA concentrations caused the polymer to become viscous and adhere to nontargeted tissues, affecting ocular application. Therefore, high concentrations of TA needed to be avoided in ocular formulations. Based on the Box-Behnken experimental results (Table S1), we derived multiple formulations with T_{gel} of 30 ± 2 °C. To balance precise sol-gel transition temperature, collagen binding capability, and minimization of visual impact, formulations containing 5 % P188, 18 % P407, and 2.5 % TA were ultimately selected for further studies. This optimized formulation exhibits light transmittance in the visible spectrum similar to pure water and, notably, showed significant better transmittance after AmB loading compared to free AmB (Fig. S2). Additionally, the selected PX-TA formulation exhibited gelation at 30.5 °C and flowability at 24 °C (Fig. 1F).

AmB is a highly potent antifungal drug with extremely poor solubility in both organic solvents and water [45]; additionally, it lacks clinically available ophthalmic formulations with traditional forms, such as deoxycholate solutions and aqueous suspensions, that cause significant irritation and toxicity to the ocular surface [13]. AmB was loaded into PX-TA to synergistically enhance antimicrobial efficacy alongside TA, and no significant changes were observed in the properties of the hydrogel after loading. AmB is soluble in DMF, and AmB-loaded PX micelles were prepared via the thin film hydration method. The micelle size was 65.5 ± 6.2 nm, as determined by dynamic light scattering (DLS) (Fig. S1C). The AmB-loaded hydrogel PX-TA-AmB was obtained by mixing AmB-loaded PX micelles with TA. The drug loading of AmB in PX-TA-AmB hydrogel is 0.19 wt% as determined by UV–vis spectrophotometer with a high encapsulation efficiency is 95 %. It should be noted that AmB is a highly potent antifungal drug, with a minimal inhibitory concentration of 0.5 μg/mL to *Candida albicans* [46], while AmB concentration in PX-TA-AmB (1.9 mg/mL) is much higher than this value. Scanning electron microscopy (SEM) imaging revealed the highly porous macrostructure of PX-TA (Fig. 1G), which remained largely unchanged after AmB encapsulation (Fig. S3).

The drug release profiles of AmB from PX-TA-AmB and AmB (0.2 % suspension) were determined by in vitro drug release experiments. AmB suspension release AmB and plateaued quickly within 1 h. While PX-TA-AmB eliminated the burst release, significantly prolonged the release of AmB and plateaued at 12 h (Fig. S4). Additionally, stability is crucial for the clinical translation of ophthalmic formulations. The stability of PX-TA-AmB was confirmed through visual appearance, sol-gel transition temperature, and in vitro antifungal efficacy assessments. PX-TA-AmB demonstrated excellent stability over a 28-day period, whereas free AmB gradually precipitated and showed significantly reduced in vitro antifungal activity by day 28 (Fig. S5).

The rheological behaviors of PX (18 % P407, 5 % P188), PX-TA (18 % P407, 5 % P188, 2.5 % TA), and PX-TA-AmB (18 % P407, 5 % P188, 2.5 % TA, 0.2 % AmB) under simulated ocular conditions were compared. All formulations demonstrated temperature-dependent rheological behavior, with T_{gel} values of 35.04 °C, 30.54 °C, and 30.04 °C, respectively (Fig. 1H). Additionally, the viscosities at the corresponding temperatures were 3968.1 mPa·s (PX at 35.04 °C), 13511 mPa·s (PX-TA at 30.54 °C), and 13143 mPa·s (PX-TA-AmB at 30.54 °C) (Fig. 1I); these results indicated significantly increased viscosity in PX-TA. However, at temperatures less than 24 °C, all three formulations presented viscosities less than 300 mPa·s; thus, they were suitable for administration as eye drops at room temperature.

To simulate blinking motion, large-amplitude oscillatory shear rheology testing was performed by cycling between 1 % and 50 % strain to evaluate the structural recovery properties of PX-TA-AmB (Fig. 1J). The results demonstrated that the liquid state of PX-TA-AmB during eye closure (50 % strain) prevented foreign body sensation and discomfort, and the corneal gaps under damaged conditions were more effectively filled. During eye opening (1 % strain), the gel state increased the ocular surface retention time of PX-TA-AmB. These findings confirmed the successful development of a thermosensitive hydrogel eye drop suitable for drug delivery to damaged corneal tissue; therefore, a comprehensive in vitro and in vivo evaluation of its therapeutic efficacy was warranted.

2.2. Adhesion analysis of the PX-TA-AmB eye drops to corneal ulcers

Due to the high affinity of the catechol and gallic acid groups of TA for collagen, coupled with extensive collagen exposure during corneal ulcer formation, we hypothesized that PX-TA-AmB would strongly adhere to and remain at corneal ulcer sites. To validate this hypothesis, anterior segment optical coherence tomography (AS-OCT) and an in vivo imaging system (IVIS) were used to evaluate the gel dynamics and retention characteristics of PX-TA-AmB eye drops in a standardized rabbit model featuring a 2.5 mm central corneal stromal defect. Additionally, ex vivo porcine corneas (with intact or debrided epithelium) were utilized to assess the collagen-binding capacity of PX-TA-AmB and PX through IVIS.

AS-OCT imaging at 90 min revealed significant gel retention at the

corneal defect site in the PX-TA-AmB group (56.14 ± 2.25 %); this value was approximately 5.58-fold greater than that in the PX group (10.06 ± 2.07 %) and 25.17-fold greater than that in the Tobrex® control group (2.23 ± 0.70 %) (Fig. 2A–C). In contrast, the PX hydrogel exhibited rapid clearance within 30 min (17.39 ± 3.04 %), and its retention rates were inferior to those of conventional Tobrex® ointment (28.27 ± 3.14 %). Based on the false-color AS-OCT images, over time, the reflectance density of the PX-TA-AmB hydrogel increased (Fig. 2B). This observation indicated that the hydrogel underwent dehydration, leading to a gradual concentration and an increase in mechanical strength. These AS-OCT results highlighted the significant capacity of PX-TA-AmB to achieve sustained retention at corneal defect sites.

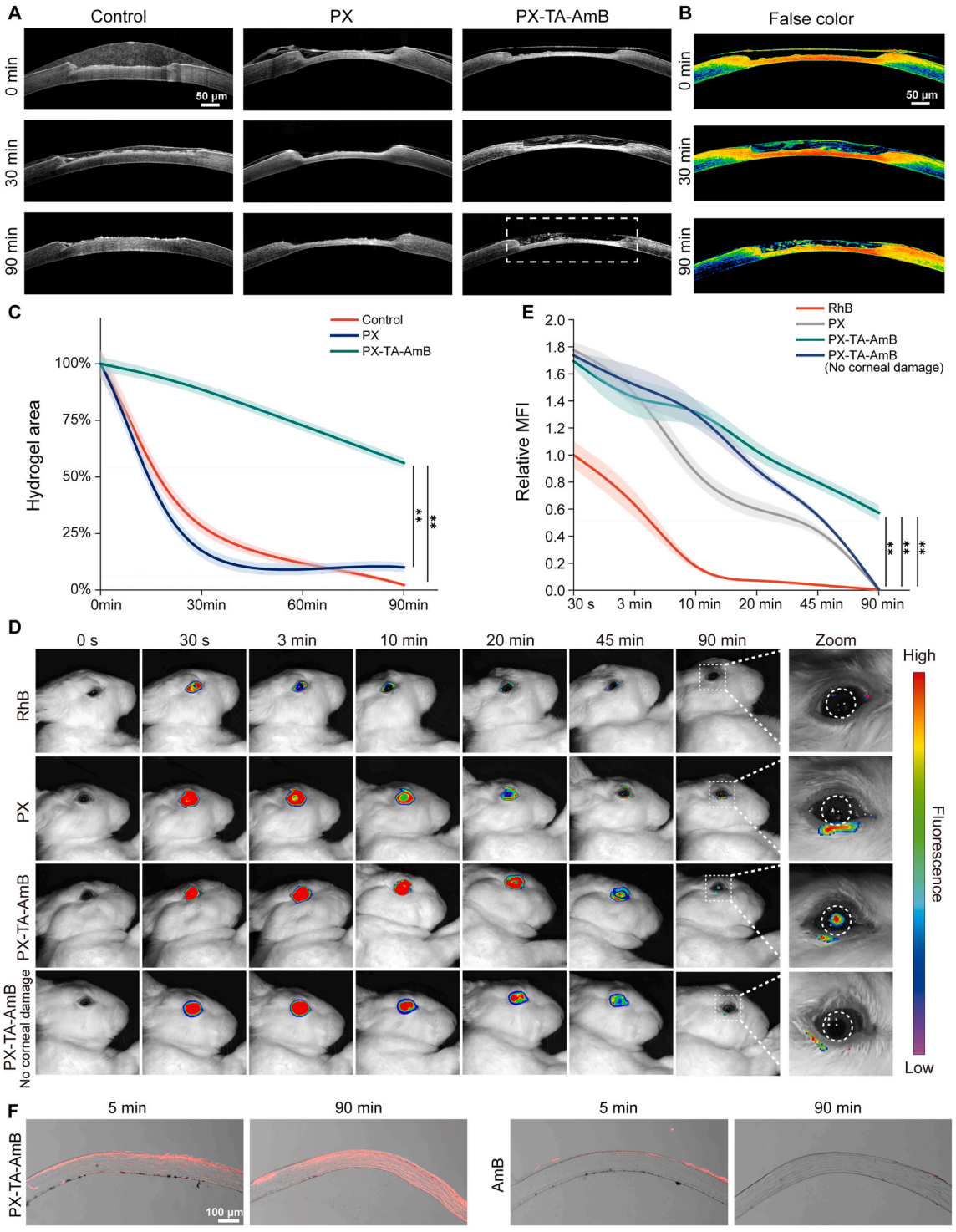

Fig. 2. Adhesion ability of PX-TA-AmB eye drops on corneal ulcers. (A–C) Visualization of the gel behavior in injured corneas, including (A) representative OCT images, (B) representative false color OCT images of PX-TA-AmB eye drops, and a (C) line plot showing the amount of remaining hydrogel on corneal surfaces over time. (D) Representative in vivo fluorescence images of the effects of RhB, PX, and PX-TA-AmB administration in injured corneas and PX-TA-AmB administration in intact corneas (white dashed circles indicate corneal regions), along with (E) quantitative assessment of fluorescein intensity on rabbit corneal surfaces at different time points. (F) Fluorescence images of mouse corneal frozen sections at different time points after administration of AmB and PX-TA-AmB with Cy3 dye loading. $^{*}P < 0.05$, $^{**}P < 0.01$, $^{***}P < 0.001$, $^{****}P < 0.0001$. Mean ± SD, $n = 3$; two-way ANOVA.

IVIS fluorescence analysis using Rhodamine B (RhB) further validated these findings (Fig. 2D and E). At 90 min, fluorescence signals were exclusively detected in the defective corneas treated with PX-TA-AmB (0.572 ± 0.06), whereas the fluorescence signals nearly disappeared at 90 min (0.005 ± 0.0004) when PX-TA-AmB was applied to intact corneas. Conventional RhB eye drops produced fluorescence signals that were difficult to detect after 10 min because of tear clearance, whereas the PX formulations accumulated on the eyelids after 45 min and failed to come in direct contact with the cornea to exert therapeutic effects. In the in vitro IVIS experiments with porcine corneas, including both debrided and intact corneal epithelia, PX-TA-AmB demonstrated superior corneal retention capabilities compared to PX alone after 30 min of PBS washing. Moreover, PX-TA-AmB exhibited significantly enhanced adhesion to corneas with debrided epithelia, revealing its binding ability to exposed collagen following corneal injury (Fig. S6). These IVIS results further confirmed the collagen-binding capacity of PX-TA-AmB in damaged corneas.

Since fungal keratitis often involves infection of the deep corneal stroma, drug penetration and retention within the stromal layer are crucial. We used the hydrophobic dye Cy3 as a tracer in place of AmB to visualize the penetration and retention of encapsulated drugs through epithelium-debrided mouse corneas. Fluorescence imaging at 5 min demonstrated that PX-TA-AmB exhibited significantly superior corneal retention compared to free AmB. This difference became even more pronounced at 90 min, when free AmB showed almost no retention in the cornea, while PX-TA-AmB remained clearly visible and had penetrated the entire cornea (Fig. 2F).

The increased retention time of ophthalmic formulations directly correlated with therapeutic efficacy, particularly in corneal diseases. AS-OCT and IVIS results demonstrated that PX-TA-AmB thermosensitive eye drops formed uniform gels at physiological temperature and maintained prolonged retention (>90 min) at corneal defect sites; this retention significantly exceeded the retention thresholds of both the conventional adhesive ophthalmic in situ gels (<30 min) [37–40] and the commercial mucoadhesive eye drops (approximately 15 min) [47]. Additionally, compared with healthy corneas, PX-TA-AmB exhibited significant collagen-binding properties and enabled prolonged retention in corneal ulcer-like craters. This binding advantage stems from the abundant catechol and gallic acid groups of TA. As reported, TA primarily interacts with collagen through hydrogen bonding, with additional contributions from electrostatic and hydrophobic interactions [48]. This corneal retention capability of PX-TA-AmB was further confirmed in fluorescence tracing studies using epithelium-debrided mouse corneas, where the extended corneal retention time significantly improved corneal penetration and stromal retention. Due to the prevalence of corneal ulcers in corneal diseases, PX-TA-AmB could provide targeted and unexpected therapeutic benefits for collagen-exposed conditions, such as keratitis and dry eye, and could be used to further establish TA-based bioactive materials as promising platforms for ocular drug delivery.

2.3. In vivo pharmacokinetics study

The pharmacokinetic evaluation of PX-TA-AmB was conducted on rabbits, with AmB (0.20 % suspension) as a contrast (Fig. S7). After treated by PX-TA-AmB or AmB (0.20 % suspension), the cornea and aqueous humor of rabbits were collected and AmB concentration was determined by HPLC. The pharmacokinetic parameters were calculated by Phoenix WinNonLin 8.1 software. The AmB concentration in PX-TA-AmB treated group was much higher than AmB treated group, both in cornea and aqueous humor. The C_{max} of PX-TA-AmB treated cornea was 30.55 μg/g, 6.47-fold of that in AmB suspension treated cornea. The $AUC_{0-\infty}$ of PX-TA-AmB in cornea is 116.14 h·μg/g, and is 9.8-fold higher than compared to 10.75 h·μg/g in AmB suspension. The $T_{1/2}$ of PX-TA-AmB in cornea (6.65 h) was also much longer than AmB suspension (0.8 h).

2.4. In vitro antifungal activity and anti-biofilm capability of PX-TA-AmB

TA not only enhances the adhesion of hydrogel systems but also plays a pivotal role in the design of antimicrobial biomaterials because of its potent and broad-spectrum antimicrobial properties. The antifungal capabilities of the different groups were assessed using colony-forming unit (CFU) determination, fungal survival assays, and fungal disc diffusion assays. The CFU images illustrate the antibacterial effects of PX-TA-AmB and other treatments (Fig. 3A). In the fungal survival assay (Fig. 3D), unlike its antibacterial properties, the AmB-free PX-TA hydrogel exhibited weak antifungal activity (with over 70 % fungal survival). In contrast, the AmB-loaded PX-TA-AmB hydrogel eliminated nearly all fungi and significantly outperformed the free AmB group; despite being a potent clinical fungicide, the free AmB group still allowed approximately 50 % fungal survival. The disc diffusion assay results corroborated these findings, and PX-TA-AmB demonstrated an inhibition zone approximately twice the diameter of AmB (Fig. 3B and C). Noteworthy, compared to AmB, PX-TA and PX-TA-AmB demonstrated enhanced biofilm-disrupting capabilities. Specifically, the binding of crystal violet to extracellular polymers revealed varying biofilm inhibitory effects across the different groups, and the PX-TA and PX-TA-AmB treatments significantly reduced the amount of extracellular polymers in the biofilms and showed notable inhibition rates (Fig. 3E). In the SYTO9-stained 3D confocal images (Fig. 3F), the control group's green fluorescence signal was dense and intact, whereas AmB disrupted part of the biofilm; this led to a sparser green fluorescence signal and a significant, though still unsatisfactory, reduction in biofilm volume. PX-TA already exhibited good biofilm resistance, while AmB-loaded PX-TA-AmB had the strongest biofilm-inhibiting effect, with minimal green fluorescence signals present and a biofilm volume approaching zero (Fig. 3G and H). SEM images of *Candida albicans* further confirmed the antifungal effects of PX-TA-AmB (Fig. 3I). Under PX-TA and PX-TA-AmB treatment, fungal spores exhibited shrinkage and disrupted morphology, whereas spores in the control group adhered to the extracellular matrix, indicating a tendency to form biofilms. In contrast, AmB treatment caused only the spores to shrink.

The excellent biofilm resistance of PX-TA and PX-TA-AmB was attributed to TA acting as a multidentate ligand, binding to proteins through strong hydrophobic interactions and hydrogen bonding; these interactions inhibited the microbial metabolism and simultaneously disrupted the biofilms. TA-modified PX-TA exhibited excellent antibacterial and antibiofilm properties, and its potential mechanisms involved metal chelation, inhibition of cell wall synthesis, and damage to the cell membrane. In contrast, the fungicidal mechanism of AmB involves binding to ergosterol in fungal cell membranes, forming pores that lead to fungal cell death. Nearly all polyphenolic compounds, including TA, demonstrated strong antibacterial activity but relatively weak antifungal properties, possibly due to the more complex cell wall composition of fungi; however, thorough eradication of pathogens is crucial in combating microbial infections. Based on the different antimicrobial mechanisms of TA and AmB, the loading of AmB onto PX-TA synergistically enhanced antifungal and antibiofilm effects while reducing the required concentration of AmB. This complementary integration highlights the strategic advantage of loading AmB onto the PX-TA platform for effective FK treatment.

2.5. In vivo efficacy of the fungal keratitis treatment

Animal models of FK were established to evaluate the therapeutic effects of PX-TA-AmB with prolonged ocular surface retention in FK (Fig. 4A). In preliminary studies, we compared anterior segment photography, fluorescein sodium staining, and Hematoxylin and eosin (H&E) staining results between AmB and natamycin administration (Fig. S8). Natamycin (clinically used drug for FK) demonstrated inferior therapeutic effects compared to AmB; therefore, AmB was selected as the positive control group.

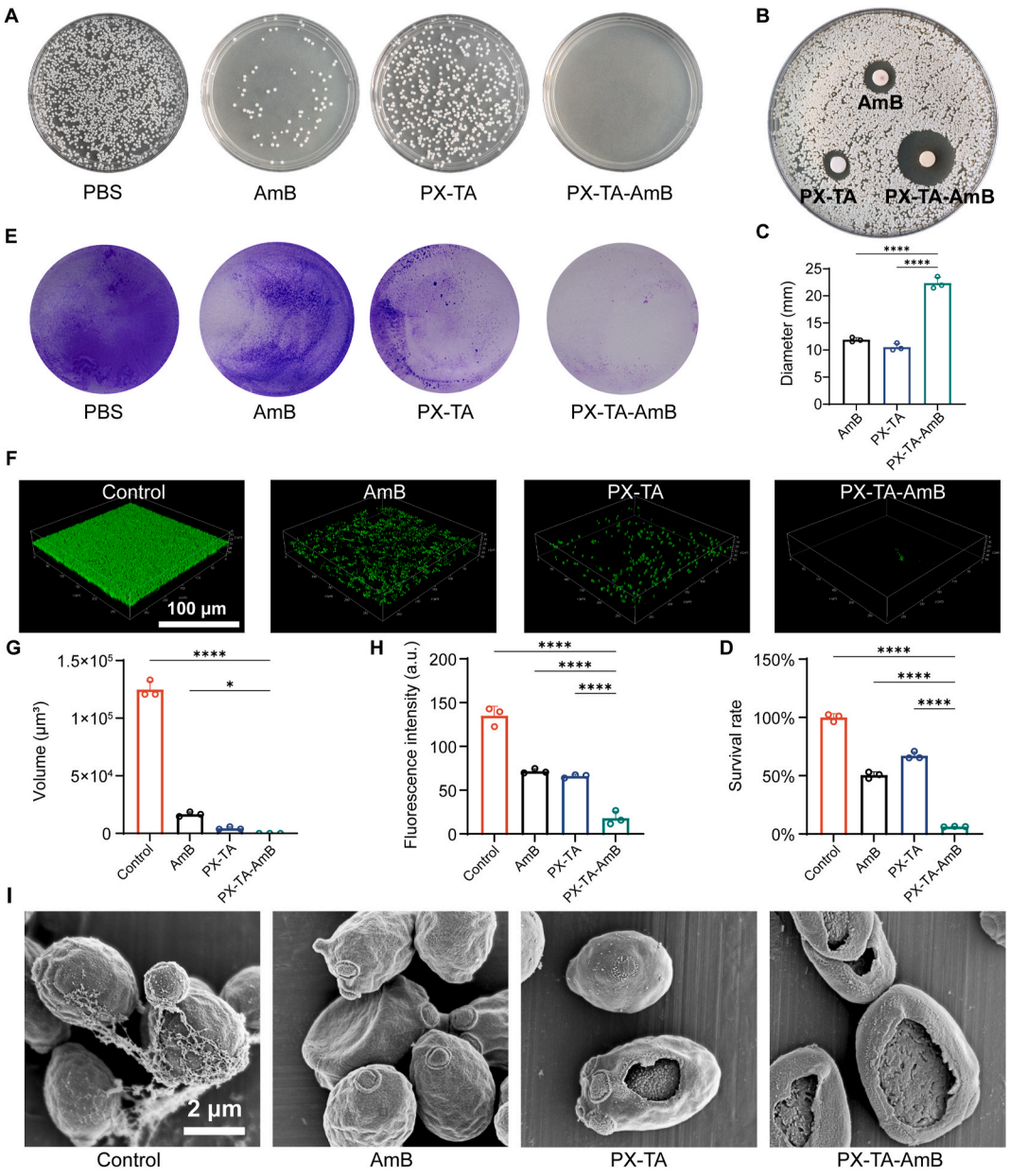

Fig. 3. Antifungal and antibiofilm capabilities of PX-TA-AmB in vitro. (A) Representative colony images of *Candida albicans*. (B) Kirby–Bauer disk diffusion assay and (C) statistical analysis of the results after different eye drop administrations. (D) Corresponding quantification of fungal viability. (E) Representative crystal violet-stained biofilm images after different eye drop administrations. (F) Representative SYTO9-stained 3D confocal images of the *Candida albicans* biofilm after different eye drop administrations. (G) Biofilm volume and (H) fluorescence intensity after different administrations. (I) Representative SEM images of the *Candida albicans* after different eye drop administrations. $^{*}P < 0.05$, $^{**}P < 0.01$, $^{***}P < 0.001$, $^{****}P < 0.0001$. Mean ± SD, $n = 3$; one-way ANOVA.

At 24 h post infection with *Candida albicans*, corneal infection-related symptoms, including corneal edema and cloudiness, were observed (Fig. 4B and C). In the control and PX groups, these symptoms progressively worsened, reaching peak disease scores on day 4 (11.40 ± 0.55 in the control group and 11.00 ± 0.71 in the PX group); these high disease scores were characterized by corneal edema, cloudiness, and perforation, with no relief throughout the observation period. In contrast, the other three groups showed varying degrees of improvement in corneal inflammation. However, the therapeutic effect in the AmB group, which was administered six times daily as a positive control for the clinical regimen, was limited, and corneal inflammation progressed to significant opacity and edema by day 10 (7.40 ± 1.14). PX-TA substantially improved therapeutic outcomes and effectively controlled corneal inflammation as early as day 4 (7.00 ± 0.71), with notable reductions in residual corneal opacity by day 10 (5.20 ± 0.45). Treatment with PX-TA-AmB, which included an antimicrobial agent, further enhanced the efficacy and completely controlled inflammation by day 10 (2.00 ± 0.71), with only minimal residual opacity; this treatment significantly outperformed the other groups. Notably, fungal load assays on day 4 revealed significant antifungal effects of AmB and PX-TA-AmB (fungal survival rates: 1.39 % and 0.19 %, respectively), and both were superior to those of PX-TA (fungal survival rate: 9.96 %) (Fig. 4E). However, despite effectively eradicating almost all pathogens, the AmB group showed no reduction in corneal inflammation, indicating that the inflammatory response was not suppressed by AmB. Additionally, fluorescein sodium staining images were used to evaluate the therapeutic efficacy. As shown in Fig. 4B and D, PX-TA-AmB and PX-TA markedly repaired corneal epithelial defects; this particularly applied to the PX-TA-AmB group, which showed almost no fluorescein sodium staining in the corneal epithelium.

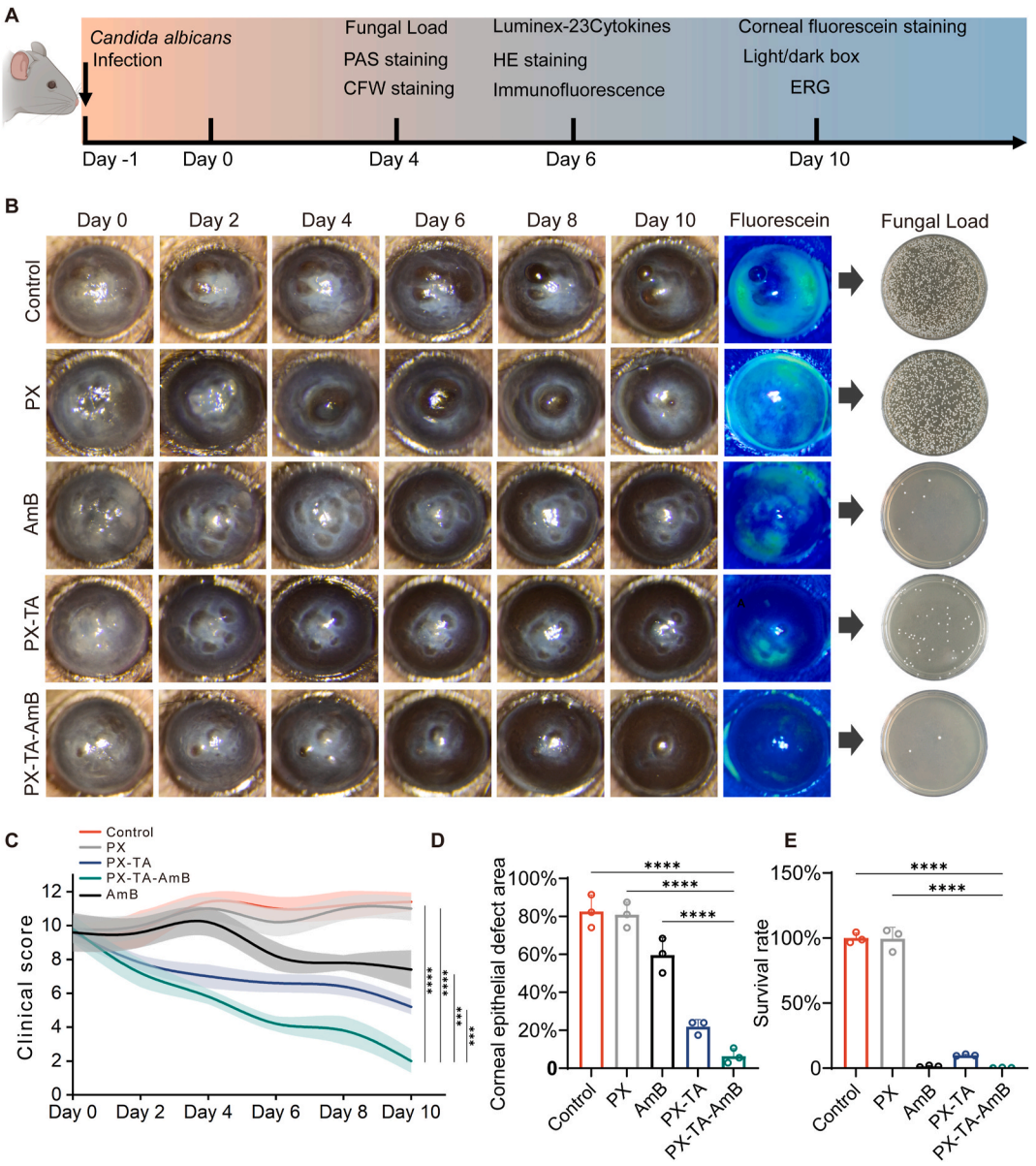

Fig. 4. In vivo efficacy of PX-TA-AmB on FK. (A) Schematic of the modeling and intervention process in an in vivo mouse FK model. (B) Representative images of the anterior segment (at different time points), cobalt blue images after fluorescein sodium staining (day 10), and fungal load assays in the corneal tissues of the corresponding groups (day 4). (C) Corneal clinical scores ($n = 5$). (D) Quantitative analysis of the fluorescein sodium staining in the corneal area ($n = 3$). (E) Statistical analysis of the fungal load ($n = 3$). $^{*}P < 0.05$, $^{**}P < 0.01$, $^{***}P < 0.001$, $^{****}P < 0.0001$. Mean ± SD, one-way ANOVA test.

Visual function is an important clinical indicator of corneal disease severity. Unlike human conditions, subjective assessments of visual symptoms such as photophobia and visual impairment (key clinical symptoms of FK) are difficult to perform in animal models; therefore, these indicators are often disregarded by researchers [49]. In this study, a light/dark box test is used on Day 10 to evaluate photophobia under different treatments. Mice are sensitive to photophobia, which drives them to stay in the dark compartment to avoid light, as shown in the schematic diagram (Fig. 5A). The activity trajectories of the mice under different treatments are presented as heatmaps (Fig. 5B), and the corresponding time spent in the light/dark box was recorded (Fig. 5C). The control group showed a significant preference for the dark compartment; these results indicated severe photophobia. The other groups, particularly the PX-TA and PX-TA-AmB groups, exhibited substantial relief from photophobia, with levels comparable to those of healthy mice. Based on these results, PX-TA and PX-TA-AmB eye drops have the potential to improve visual function following corneal disease, potentially because the thermosensitive eye drops are able to fill many corneal defects, allowing the cornea to maintain a curvature similar to that of a healthy cornea even after disease. Visual impairment is another important indicator of visual function and was indirectly assessed via electroretinogram (ERG) across groups (Fig. 5D, E, F). The control group presented decreased a-wave and b-wave amplitudes, whereas the amplitudes in the PX-TA-AmB group returned to normal levels after treatment. This improvement could be attributed to the transparent cornea allowing light transmission.

Overall, PX-TA-AmB demonstrated comprehensive therapeutic efficacy in addressing posttreatment complications of FK due to the dual functionality of TA in terms of anti-inflammatory and antifungal properties. Notably, while conventional clinical management of FK typically requires antifungal administration every 15 min, once-daily administration of PX-TA-AmB resulted in superior therapeutic outcomes compared with six-times-daily AmB treatment. The enhanced efficacy could be attributed to the collagen-binding properties of PX-TA-AmB,

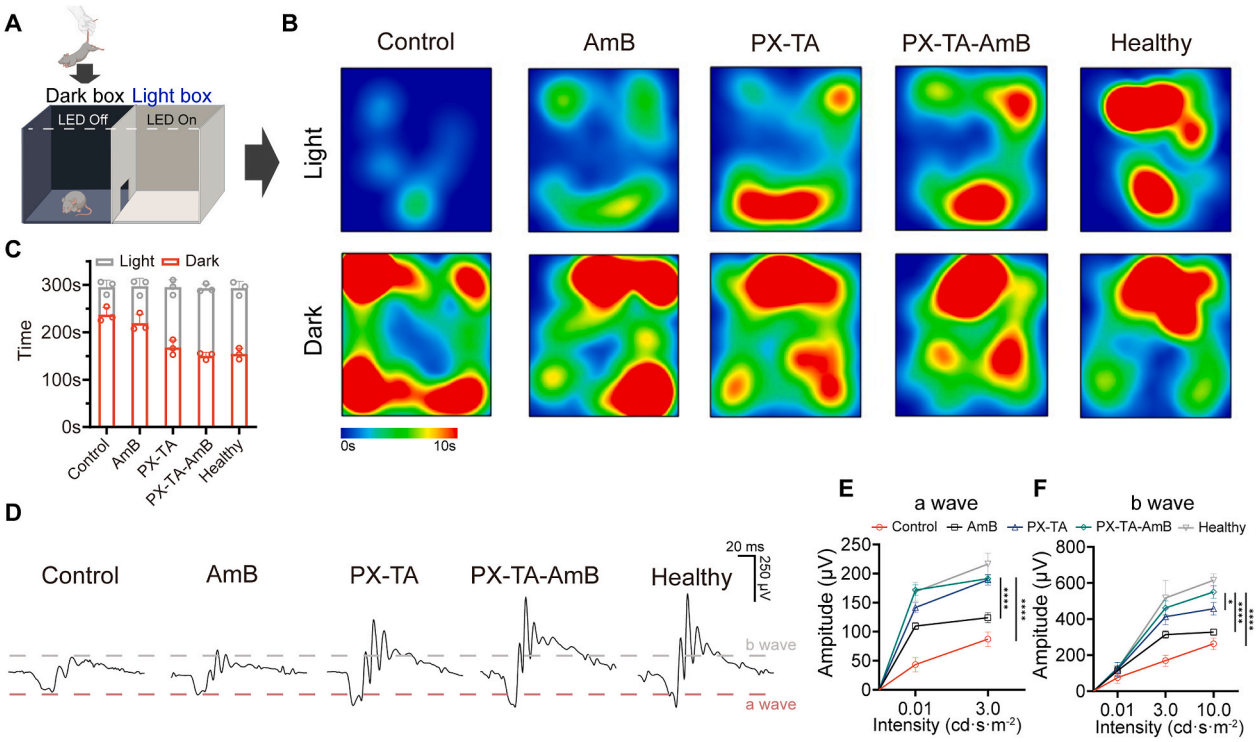

Fig. 5. Ethological and visual function analysis. (A) Schematic of the light–dark box and (B) representative heatmap of the movement trajectories of mice subjected to different administrations in the light–dark box test, along with (C) corresponding quantitative analysis of the amount of time spent in the light–dark box. (D) Electroretinogram (ERG) graphs and (E, F) corresponding statistical analysis of a- and b-wave amplitudes after different eye drop administrations. $^{*}P < 0.05$, $^{**}P < 0.01$, $^{***}P < 0.001$, $^{****}P < 0.0001$. Mean ± SD, $n = 3$; one-way ANOVA.

which significantly prolonged the corneal retention time. This once-daily eye drop regimen would significantly improve patient compliance, thereby addressing the poor therapeutic outcomes resulting from compliance issues. Together, these advantages demonstrate the promising potential of PX-TA-AmB as a clinically translatable therapeutic strategy for effective FK management.

2.6. Histological and cytokine analyses

Histopathology and cytokine analysis were performed to evaluate the anti-inflammatory and antifungal effects. To better evaluate the expression levels of various cytokines, corneas from each group were collected on day 6 for protein level analysis of 23 cytokines using the Luminex system. The cytokine levels are shown in Fig. 6A. PX-TA and PX-TA-AmB significantly suppressed the expression of 22 inflammatory and chemotactic cytokines, with the exception of TNF-α, and the protein levels approached those of healthy mice. Conversely, AmB treatment significantly suppressed only the protein expression of IL-6, IL-17A, G-CSF, and eotaxin, whereas most cytokines remained highly expressed; these results indicated that the inflammatory cytokine storm persisted, whereas PX-TA and PX-TA-AmB eye drops effectively controlled this condition. Additionally, the immunofluorescence results of IL-1β and IL-6, which are key cytokines, further confirmed the anti-inflammatory effect of PX-TA-AmB (Fig. 6F, G and S10).

H&E staining was used to evaluate corneal morphology and inflammatory cell infiltration after treatment. As shown in Fig. 6B and C, the corneal stroma in the control group was severely infiltrated by the inflammatory cells, with significant morphological disruption, increased thickness due to edema, and epithelial detachment. Treatment alleviated these conditions to varying extents. Compared with the control group, the AmB group presented less corneal stromal damage, but the level of inflammation and corneal thickness did not improve, likely due to the antifungal effects of AmB; these effects limited fungal damage but had a minimal effect on pathogen-induced inflammation. In contrast, PX-TA and PX-TA-AmB significantly reduced inflammatory cell infiltration, restored corneal thickness, and preserved an intact corneal epithelial structure. However, stromal damage was still present in the PX-TA group, likely due to the absence of antifungal agents, highlighting the necessity of antifungal drug loading in PX-TA. Notably, the H&E staining results for the AmB group and the control group were more severe on day 10 posttreatment (Fig. S9), and persistent inflammatory cell infiltration, iris adhesion, extensive corneal scarring, and corneal neovascularization were observed in both groups. Consistent with the fungal load results, periodic acid–Schiff (PAS) staining revealed abundant fungal hyphae in the corneal stroma of the control group and confirmed the superior fungal eradication ability of PX-TA-AmB with respect to the other groups (Fig. 6D). Calcofluor white (CFW) staining further enhanced the visibility of the fungal structures through fluorescent labeling (Fig. 6E). On the other hand, timely healing of the corneal epithelium following trauma, microbial infection, or surgical injury is crucial for corneal restoration [50]. Notably, PAS staining revealed that PX-TA-AmB treatment eradicated most fungi, confined them to the epithelial layer, and led to normal corneal epithelial repair rather than the abnormal proliferation, as observed in the AmB group; here, the abnormal epithelial proliferation caused by AmB treatment was a contributing factor to corneal opacity.

2.7. Potential mechanisms of PX-TA-AmB in treating fungal keratitis

Although polyphenol-based biomaterials and free polyphenolic compounds have been extensively validated for their efficacy against FK [51,52], their underlying mechanistic pathways remain insufficiently investigated. Due to the remarkable therapeutic efficacy of PX-TA-AmB across multiple aspects of FK treatment, we conducted subsequent experiments to elucidate its potential molecular mechanisms. Transcriptomic analysis via mRNA sequencing was performed to investigate

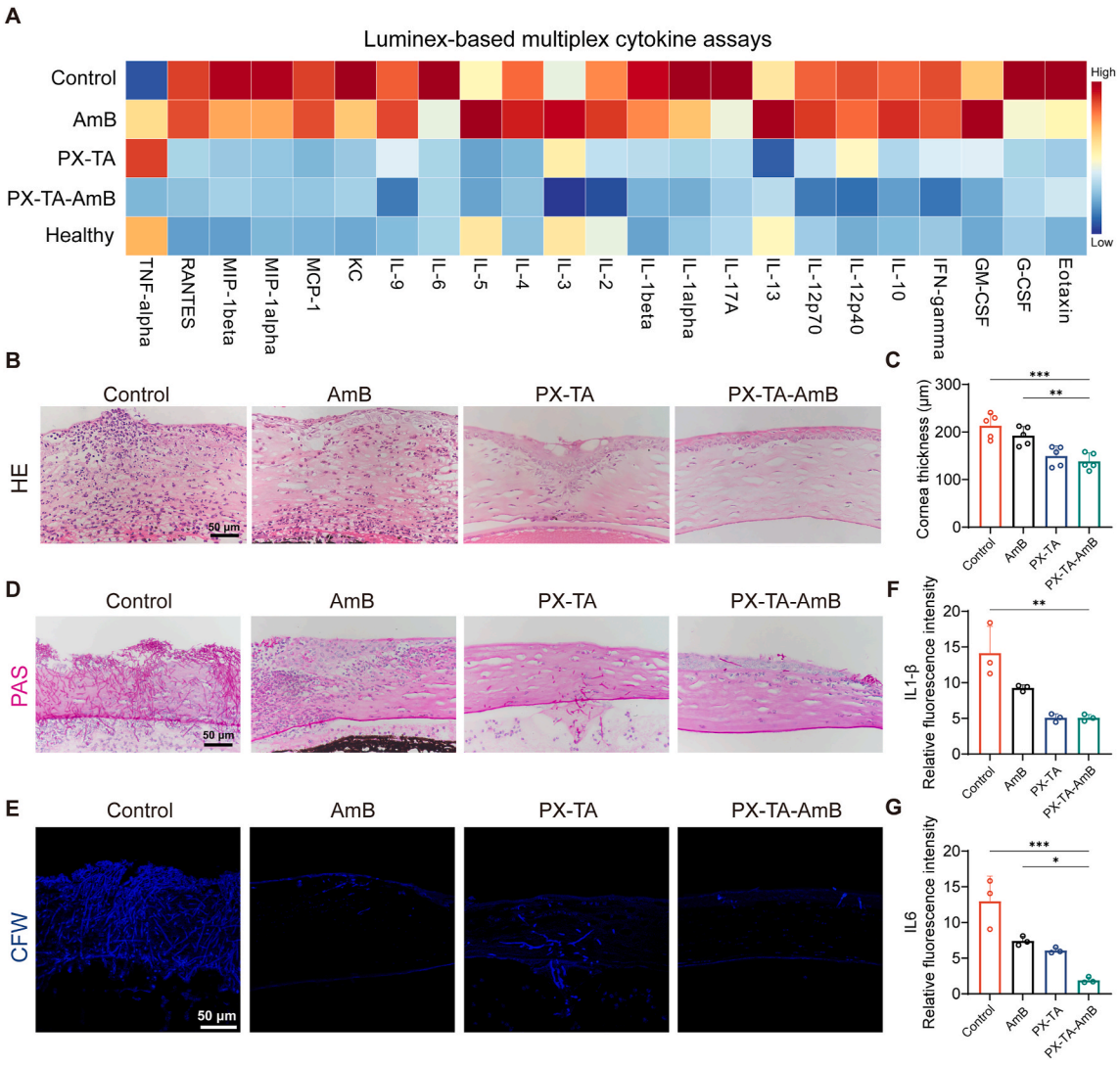

Fig. 6. Histological evaluation and anti-inflammatory efficacy of PX-TA-AmB in vivo. (A) Luminex-based assay of the 23 cytokine protein expressions after different eye drop administrations. (B) Corneal H&E staining after different eye drop administrations and (C) corresponding quantitative analysis of corneal thickness ($n = 5$). (D) Corneal PAS staining and (E) calcofluor white (CFW) staining to visualize fungal hyphae in the cornea. (F) Quantitative analysis of IL-1β and (G) IL6 immunofluorescence-positive areas in the cornea ($n = 3$). $^{*}P < 0.05$, $^{**}P < 0.01$, $^{***}P < 0.001$, $^{****}P < 0.0001$. Mean ± SD, one-way ANOVA test.

the therapeutic mechanisms of PX-TA-AmB in FK. Comparative analysis of corneal gene expression before and after PX-TA-AmB treatment revealed 2363 differentially expressed genes (DEGs); these consisted of 583 upregulated and 1780 downregulated genes (Fig. 7A). Kyoto encyclopedia of genes and genomes (KEGG) enrichment analysis demonstrated the crucial role of the PI3K/AKT signaling pathway in PX-TA-AmB-mediated FK treatment and corneal repair (Fig. 7B); these results were further validated by gene ontology (GO) analysis (Fig. S11). DEGs related to the inflammatory response, signaling pathway regulation, and corneal scarring are further illustrated in the heatmap (Fig. 7C). As shown in Fig. 7F–H and Fig. S12, PX-TA-AmB treatment significantly downregulated the mRNA expression of the genes associated with corneal injury (α-SMA, LOX, VIM, MMP9, FN1, and ITGB1), the key inflammatory cytokines (IL6 and IL1B), and the pathway regulators (MAPK6, PIK3CD, and PIK3R6). Further gene set enrichment analysis (GSEA) using KEGG and REACTOME gene sets revealed that PX-TA-AmB treatment significantly downregulated both the PI3K/AKT signaling pathway and fibrotic processes related to collagen synthesis and assembly (Fig. 7D and E).

First, transcriptomic analysis revealed that PX-TA-AmB treatment significantly contributed to inflammation suppression, corneal injury repair, and scar formation inhibition in FK. Based on these comprehensive findings, we hypothesized that the PI3K/AKT signaling pathway, which plays crucial roles in the inflammatory response, immune regulation, and wound healing and is hyperactivated in FK, serves as a key mediator of these therapeutic effects. Among the significantly altered DEGs, MAPK6 (Fig. 7F), which is an atypical member of the MAPK family whose molecular mechanisms are not fully understood, was notably upregulated in FK. In tumor studies, MAPK6 overexpression has been shown to phosphorylate AKT at the S473 site [53]. Our transcriptomic analysis preliminarily revealed the potential existence of this regulatory mechanism in FK. Subsequent Western blot analysis confirmed that MAPK6 overexpression in the mouse FK model occurred simultaneously with increased AKT phosphorylation (Fig. 7I). Importantly, PX-TA-AmB effectively regulated MAPK6 overexpression and the phosphorylation levels of PI3K and AKT; they were restored to levels comparable to those in healthy corneas (Fig. S13). IL-1β and MMP9 are important mediators of inflammation and scar formation. It was demonstrated that PX-TA and PX-TA-AmB effectively downregulated the overexpression of IL-1β and MMP9 in FK, consistent with the transcriptomic results (Fig. 7J). Furthermore, topical administration of the AKT activator SC79 (10 μg/mL) reversed the downregulation of IL-1β

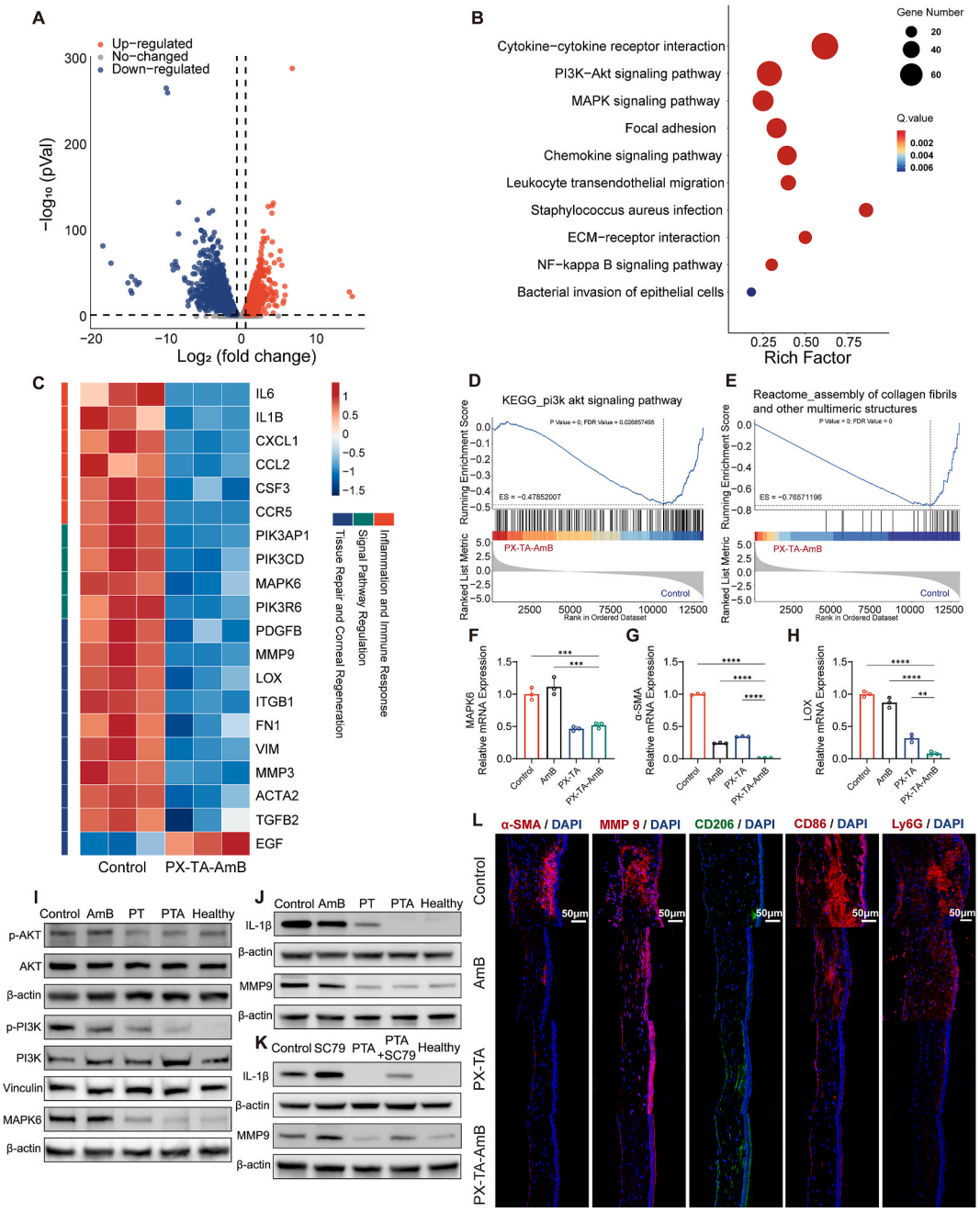

Fig. 7. Therapeutic mechanism of PX-TA-AmB in FK via MAPK6/PI3K/AKT pathway modulation. (A) Volcano plot of the differentially expressed genes. (B) KEGG pathway enrichment analysis of the differentially expressed genes. (C) Heatmap of the differentially expressed genes related to the inflammatory response, signaling pathway regulation, and corneal scarring before and after PX-TA-AmB treatment. (D, E) GSEA with the indicated KEGG and Reactome gene sets. (F, G, H) MAPK6, α-SMA, and LOX mRNA expression levels in treated versus control corneal tissues. (I) Representative Western blot images of p-AKT, AKT, p-PI3K, PI3K, MAPK6, Vinculin, and β-actin proteins in different treatment groups. (J) Representative Western blot images of IL-1β and MMP9 in different treatment groups. (K) Representative Western blot images for functional validation of the role of AKT pathway in PX-TA-AmB-mediated downregulation of IL-1β and MMP9 using the AKT activator SC79. (L) Immunofluorescence assessment of α-SMA, MMP9, CD206, CD86, and Ly6G under different treatments. $^{*}P < 0.05$, $^{**}P < 0.01$, $^{***}P < 0.001$, $^{****}P < 0.0001$. Mean ± SD, $n = 3$; one-way ANOVA.

and MMP9 expression by PX-TA-AmB and PX-TA in the FK model, indicating that the downregulation of IL-1β and MMP9 is partially mediated through the AKT signaling pathway (Fig. 7K and S14). These findings explain the excellent anti-inflammatory effects of PX-TA and PX-TA-AmB in FK treatment and provide insights into the mechanism by which PX-TA-AmB and other TA-based biomaterials exert their therapeutic effects on FK.

Next, immunofluorescence staining of different key markers was performed on mouse corneas before and after treatment (Fig. 7L). The results revealed a significant reduction in Ly6G throughout the corneal layers and indicated that PX-TA and PX-TA-AmB inhibited neutrophil infiltration in FK. The significant imbalance between CD86 and CD206 indicated that PX-TA and PX-TA-AmB inhibited macrophage activation to the M1 type (CD86 marker) while promoting a shift toward the M2 type (CD206 marker), thereby reducing the release of inflammatory cytokines. The inhibition of MMP9 and α-SMA confirmed their roles in preventing damage and promoting repair. MMP9, which is a confirmed corneal injury factor in FK, was involved in stromal degradation and

inflammation. PX-TA and PX-TA-AmB significantly reduced MMP9 expression and confined it to the corneal epithelium. A similar trend observed in α-SMA detection demonstrated the scar control after PX-TA and PX-TA-AmB treatment. Furthermore, due to the outstanding performance of PX-TA-AmB in scar inhibition and the significant enrichment of the "Assembly of collagen fibrils and other multimeric structures" pathway, which plays a crucial role in fibrosis development, the following investigations focused on the antiscarring effects of PX-TA-AmB in a lamellar keratectomy wound model in New Zealand rabbits.

2.8. Assessment of the corneal wound healing capacity

Corneal scarring represents a major pathological endpoint in FK progression and significantly contributes to permanent vision loss despite successful antifungal therapy. The above investigations with the PX-TA-AmB formulation demonstrated promising therapeutic potential in both promoting corneal healing and reducing scar formation. This potential was likely caused by two mechanisms: (1) fungal clearance prevented continued tissue damage, and (2) TA-based bioactive materials modified the microenvironment at injury sites to promote healing and prevent scarring. To independently verify the anti-scarring capability of PX-TA-AmB without the confounding factor of fungal infection, we established a lamellar keratectomy model in New Zealand rabbits to evaluate its in vivo efficacy for comprehensive corneal wound healing. Using a standardized protocol (Fig. 8A), we compared four treatment groups: PBS (control), PX, PX-TA, and PX-TA-AmB. Quantitative

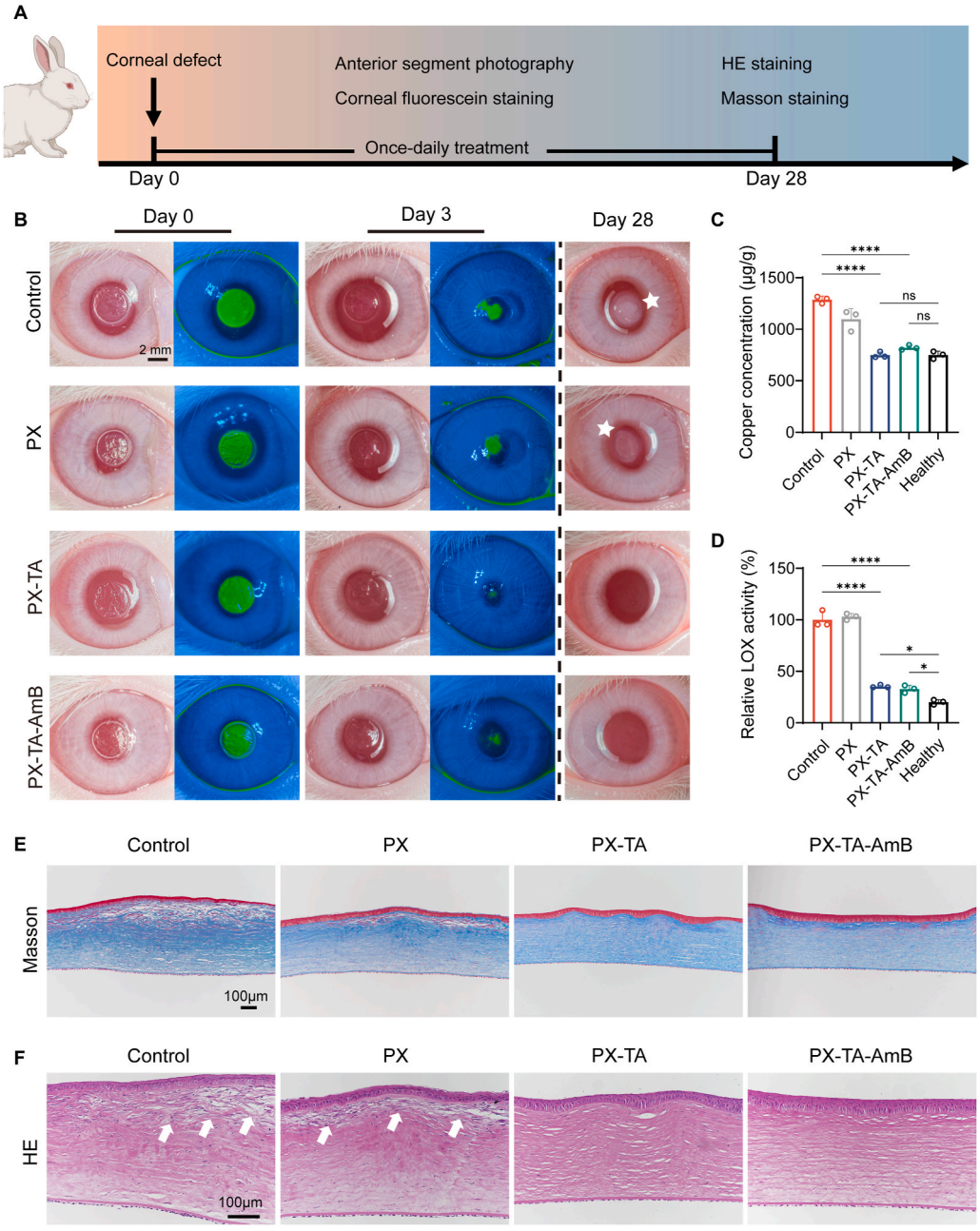

Fig. 8. Assessment of the antiscarring efficacy of PX-TA-AmB in a rabbit corneal injury model. (A) Schematic illustration of in vivo rabbit corneal injury model establishment and the intervention protocol. (B) Representative anterior segment photographs at different time points and images of fluorescein sodium staining showing significant differences under cobalt blue light (day 0, day 3) (white stars indicate areas of scarring). (C) Quantitative analysis of copper concentration and (D) fluorescence intensity analysis of LOX activity in rabbit corneas following different treatments. (E, F) Masson and H&E staining following different treatments (white arrows indicate areas of scarring). *$P < 0.05$, **$P < 0.01$, ***$P < 0.001$, ****$P < 0.0001$. Mean ± SD, $n = 3$; one-way ANOVA.

analysis of fluorescein sodium staining revealed differential healing patterns among the treatment groups (Fig. 8B and S15). On day 3 post-injury, the control and PX groups maintained substantial epithelial defects (32.18 ± 2.39 % and 29.38 ± 3.23 % of the initial wound area), whereas the PX-TA and PX-TA-AmB groups had significantly reduced fluorescence staining areas (5.43 ± 1.86 % and 7.32 ± 2.86 %, respectively); these results indicated enhanced epithelial healing capacity.

On day 28, anterior segment photography revealed marked central corneal opacity in the control and TA groups, whereas corneas treated with PX-TA and PX-TA-AmB maintained superior transparency. Pathological histology further validated these observations (Fig. 8E and F). On day 28, the control and PX groups presented prominent scarring features that were characterized by disorganized and loose collagen fibers alongside distinctly differentiated myofibroblasts. In contrast, the PX-TA- and PX-TA-AmB-treated corneas had an organized collagen arrangement with no evident scarring regions and showed features of normal corneal regeneration. The significant downregulation of α-smooth muscle actin (α-SMA, also known as ACTA2) and lysyl oxidase (LOX) mRNA expression in corneas on day 28 further supported these findings (Figure S16). Additionally, continuous 28-day administration of PX-TA and PX-TA-AmB regulated corneal copper levels to near-healthy levels and coordinately modulated LOX activity, exhibiting intermediate LOX activity levels that were lower than the control group but higher than healthy corneal tissue (Fig. 8C and D). This moderate LOX activity simultaneously fulfilled the requirements for normal corneal healing while preventing the excessive enzymatic activity that would otherwise induce fibrosis.

Mechanistically, the antiscarring effects could be attributed to the metal-chelating properties of TA. As a polyphenolic compound, TA could reduce local metal ion concentrations at injury sites [54], particularly copper ions. LOX is a copper-dependent enzyme and serves as a key mediator of tissue fibrosis [55]; here, the abovementioned downregulation of LOX expression in PX-TA-AmB-treated corneas with FK indicated that TA-mediated copper chelation could contribute to reduced scarring (Fig. 7E, G and H). The correlation between TA-mediated copper chelation and LOX expression and the reduced LOX levels verified in both rabbit corneal injury and mouse FK models provide novel mechanistic insights into the antifibrotic potential of polyphenol-based biomaterials. In combination with its established antifungal properties, this formulation represents a promising strategy for improving FK prognosis through simultaneous pathogen elimination and tissue regeneration enhancement.

2.9. Biosafety assessment

The safety and tolerability of ophthalmic formulations need to be carefully considered to ensure patient comfort and health. To achieve this goal, various methods, including corneal fluorescein sodium staining, histological evaluation of cornea and major organs, intraocular pressure (IOP) measurement, in vitro cytotoxicity assessment, and the Hen's egg test-chorioallantoic membrane (HET-CAM), were employed to assess the safety of the formulations. In mouse corneas, after 10 consecutive days of PX-TA-AmB administration, no significant difference was observed in the area of fluorescein sodium-stained positive regions between the PX-TA-AmB group and the control group (Fig. S17A). Moreover, continuous administration of PX-TA-AmB for 28 days had no significant effect on IOP (Fig. S17C). The H&E staining of cornea (after 10 and 28 consecutive days of PX-TA-AmB administration) and main visceral organs revealed no apparent structural differences compared to healthy mice (Fig. S17B and Fig. S20). In vitro, human corneal epithelial cells (HCECs) and human corneal stromal cells (HCSCs) were incubated with PX-TA-AmB, resulting in minimal propidium iodide (PI) staining, similar to that in the PBS group, and most cells were positive for calcein AM (Fig. S18). In contrast, HCECs and HCSCs treated with AmB presented significantly increased PI staining, indicating the potential cytotoxicity of AmB. The HET-CAM assay also revealed similar results (Fig. S19A); thus, the PX-TA-AmB and 0.9 % w/v NaCl treatments did not induce significant irritation, whereas the AmB treatment led to mild irritation. The use of 0.1 M NaOH, which was used as a positive control for hemorrhage, resulted in severe vascular bleeding and coagulation, whereas the use of 1 % w/v sodium dodecyl sulfate (SDS), which was used as a positive control for vasoconstriction, resulted in vessel constriction and vascular bleeding and coagulation. The corresponding irritation scores (ISs) for 0.1 M NaOH and 1 % w/v SDS were 16.78 ± 0.62 and 12.95 ± 0.25, respectively, and these results indicated extreme irritancy. However, the PX-TA-AmB and NaCl treatments did not result in any irritant responses, and the IS score after AmB treatment was 2.413 ± 0.98 and indicated mild irritancy (Fig. S19B). The potential cytotoxicity and irritancy of AmB are among the limiting factors for its clinical use, whereas the above results indicate that PX-TA-AmB has good biosafety and can be safely administered via topical routes.

3. Conclusion

In this study, we developed a pathology-inspired thermosensitive eye drop system, designated PX-TA-AmB. During corneal injury, collagen is extensively exposed, and PX-TA-AmB is able to effectively address the therapeutic challenges of FK through targeted collagen binding and multifunctional effects. Specifically, compared with conventional free AmB drop therapy, which typically results in limited corneal retention (15 min) and requires six administrations daily, PX-TA-AmB demonstrated sustained retention at corneal ulcer sites (>90 min) through specific collagen-binding interactions, and superior therapeutic outcomes were attained with once-daily administration. Mechanistically, we demonstrated hyperactivation of the MAPK6/PI3K/AKT pathway in FK and its subsequent downregulation following PX-TA-AmB treatment, resulting in comprehensive anti-inflammatory effects; these effects included suppressed M1 macrophage polarization, reduced neutrophil infiltration, and downregulation of 22 inflammatory cytokines. Additionally, our results indicated that the metal-chelating properties of TA could influence the LOX expression, potentially reduce matrix fibrosis during corneal healing, and thereby provide new insights for polyphenol-based drug delivery systems. Comprehensive analyses spanning clinical presentation, ethology, visual electrophysiology, histopathology, and molecular biology demonstrate that due to the prevalence of collagen exposure in most corneal diseases, this pathology-inspired PX-TA-AmB demonstrates promising potential for clinical translation and provides an innovative approach to increase the efficiency of corneal drug delivery.

4. Experimental section

4.1. Materials and instruments

PX 407, PX 188, TA and AmB (≥750 μg/mg) were purchased from Shanghai Aladdin Company. The Dulbecco's modified Eagle's medium/F12 (DMEM/F12) culture medium used for cell culture was purchased from Gibco.

^{1}H NMR data were acquired from a Bruker AVANCE III 400 MHz spectrometer and analyzed with MestReNova 9.0 software. FT-IR spectra were acquired from a Bruker TENSOR II spectrometer by ATR technology. The wavenumber range was from 400 cm^{-1} to 4000 cm^{-1}. DLS and ζ potential measurements were carried out on a Zetasizer nano ZS90 (Malvern Panalytical Ltd. Malvern, UK) with a He-Ne laser (633 nm). Scattered light was detected at 90°. The data were analyzed by Zetasizer software. All the measurements were repeated three times. SEM images were acquired from a Tescan Mira LMS (Tescan, Brno, Czech Republic) with an accelerator voltage of 3 kV. UV–vis spectrum of AmB was recorded in a Shimadzu UV-1800 UV–vis spectrophotometer. The detection wavelength of AmB is set to 410 nm. Standard curve was determined based on the UV absorbance of series concentrations of AmB

ranging from 0.05 μg/mL ~50 μg/mL dissolved in DMF. The drug loading of AmB in PX-TA-AmB was determined by the absorbance of UV–vis after dissolved in DMF and calculated from the standard curve. The liquid chromatographic analysis was carried out on an Agilent high performance liquid chromatography (HPLC) system (Agilent Technologies, CA, USA) with a Venusil MP C18 column (4.6 × 250 mm, 5 μm) maintained at 30 °C. The mobile phase was composed of water containing 0.73 vol% acetic acid and acetonitrile (30/70, v/v), and the flow rate was 1 mL/min. AmB was detected at a detection wavelength of 408 nm with a retention time of 6.1 min. The standard curve was y = 122.38x – 1.86 with a R^2 of 0.999.

4.2. Preparation and characterization of PX-TA-AmB thermosensitive eye drops

PX-TA was prepared through simple physical mixing. Specifically, the required amounts of P407 and P188 were accurately weighed and gradually added to cold deionized water (approximately 4 °C) under continuous stirring. The mixture was stirred at low temperature until complete dissolution and uniformity were achieved. After a homogeneous solution was obtained, TA was slowly added to the poloxamer solution under continuous stirring. The resulting PX-TA mixture was allowed to reach room temperature and then stored at 4 °C in the dark for subsequent use.

To fabricate AmB-loaded eye drops, AmB was initially encapsulated in a poloxamer via the thin-film hydration method. Briefly, 4 mg of AmB, 1800 mg of Poloxamer P407 and 500 mg of Poloxamer P188 were dissolved in 10 mL of DMF in a 250 mL flask. After the solid materials completely dissolved, the DMF was rotary evaporated under high vacuum, and a thin film formed in the flask. Then, 30 mL of deionized water was added to the flask, and AmB-loaded micelles were formed after vigorous ultrasonication. The size of the AmB-loaded poloxamer micelles was determined by DLS. The micelles were lyophilized, and the PX-TA-AmB eye drops were prepared according to the abovementioned physical mixing of lyophilized AmB-loaded poloxamer micelles and TA accordingly. PX-TA-AmB eye drops were lyophilized and characterized by ^{1}H NMR after dissolved in dimethyl sulfoxide-d_6 and FT-IR. The drug loading efficiency of PX-TA-AmB was determined by the absorbance of UV–vis at 410 nm after dissolved in DMF and calculated from the standard curve. The drug loading was calculated according to the following formula: $DL\% = m_{AmB}/m_{hydrogel} \times 100$ %. The encapsulation efficiency was calculated according to the following formula: $EE\% = (loaded\ m_{AmB})/(fed\ m_{AmB}) \times 100$ %.

To characterize the morphology of the hydrogel formed from PX-TA-AmB eye drops after gelation at body temperature, the PX-TA-AmB eye drops were incubated at 37 °C for 1 h to allow sufficient gelation of the PX-TA-AmB. Then, the hydrogel was quickly frozen in liquid nitrogen and lyophilized. The lyophilized hydrogel was cross-sectioned, and the morphology of the hydrogel was characterized by SEM.

4.3. In vitro drug release experiments

Two milliliters of PX-TA-AmB and AmB (0.2 % suspension) were added into dialysis bag with a MWCO of 7000 Da ($n = 3$). The dialysis bags were incubated in 40 mL PBS containing 0.1 % Tween 80. At predetermined time intervals, 1 mL dialysis medium was taken out and replaced by 1 mL fresh PBS containing 0.1 % Tween 80. The concentration of AmB was determined by HPLC. The cumulative release of AmB was calculated according to the following formula:

$$C_m\% = 100\% \times \frac{V_e \sum_1^{n-1} C_i + V_0 C_n}{M_0}$$

where M_0 represents the amounts of AmB in the dialysis bag. V_0 is the whole volume of the release media ($V_0 = 42$ mL), V_e is the volume of the replaced media ($V_e = 40$ mL), C_n (μg/mL) represents the concentration of AmB in the nth sample.

4.4. Optimization of the thermosensitive eye drop formulation

Box–Behnken design (BBD) was used to explore the effects of the P188 (5–15 %), P407 (16–20 %), and TA (0–5 %) concentrations on the gelation temperature (T_{gel}). These concentrations were independent variables, and T_{gel} was the dependent variable. Systematic factor combinations were generated based on BBD principles (Table S2). Experimental designs and analyses were performed using Design-Expert 11 software (Stat-Ease, Minneapolis, MN, USA), and the results were fitted to a quadratic polynomial model. ANOVA was used to assess model significance and factor influence and screen the optimal formulations or concentration ranges.

4.5. Light transmittance assessment

Samples (100 μL) of ultrapure water, PX (18 % P407, 5 % P188), PX-TA (18 % P407, 5 % P188, 2.5 % TA), PX-TA-AmB (18 % P407, 5 % P188, 2.5 % TA, 0.2 % AmB), and AmB (0.2 % suspension) were transferred to a 96-well plate. Optical density (OD) measurements were recorded using a spectrophotometer across the wavelengths ranging from 400 to 700 nm. To evaluate the effect of varying TA concentrations on transparency, 50 μL aliquots of PBS, PX (18 % P407, 5 % P188), PX-$TA_{2.5}$ (18 % P407, 5 % P188, 2.5 % TA), and PX-TA_5 (18 % P407, 5 % P188, 5 % TA) were pipetted onto transparent glass slides. The slides were positioned over paper printed with the Tianjin Eye Hospital logo, with a heating device underneath maintaining the slide temperature at 37 °C. Images were captured using a Nikon Z6 camera (Nikon, Tokyo, Japan).

4.6. Stability assessment of PX-TA-AmB

For stability evaluation of PX-TA-AmB, both PX-TA-AmB (18 % P407, 5 % P188, 2.5 % TA, 0.2 % AmB) and free AmB (0.2 % suspension) were stored at 24 °C. At predetermined time points, the visual appearance of PX-TA-AmB was photographed and sol-gel transition temperatures were measured using the inverted tube method. Additionally, antifungal efficacy was assessed on Day 0 and Day 28 by treating 1 mL of fungal suspension (1×10^6 CFU/mL) with 1 μL of either PX-TA-AmB or free AmB for 24 h, followed by measuring the optical density at 600 nm (OD_{600}) using a SpectraMax M5 microplate reader to evaluate fungal survival rate.

4.7. Rheological properties of PX-TA-AmB

The vial inversion method and rheological tests were conducted to evaluate the thermosensitive and rheological properties of the eye drops. By inverting vials during the heating process at a rate of 1 °C/min, the change in flowability of the eye drops at different temperatures was observed to determine their sol–gel transition temperature. The rheological properties of PX, PX-TA, and PX-TA-AmB were analyzed using an MCR 302 rheometer (Anton Paar, USA) equipped with a 25 mm diameter plate. First, the storage modulus (G′) and loss modulus (G″) were measured as a function of temperature at a heating rate of 1 °C/min under conditions of 5 % strain and a frequency of 1 Hz for different eye drops. The viscosities of PX, PX-TA, and PX-TA-AmB were subsequently measured at a shear rate of $5/s^{-1}$. Additionally, the changes in G′ and G″ under 1 % and 50 % cyclic strains at 37 °C and a frequency of 1 Hz were measured to simulate the blinking action.

4.8. Corneal surface residency and adhesion behavior

The residency and adhesion behavior of the eye drops on the corneal surface were evaluated using anterior segment optical coherence tomography (AS-OCT; Opteva, USA) and an in vivo imaging system (IVIS;

Lumina XRMS Series III, PerkinElmer, Waltham, USA). The rabbits were anesthetized by intravenous injection of sodium pentobarbital (30 mg/kg) prior to imaging. AS-OCT images were captured at 0, 30, and 90 min following administration for the control group, PX group, and PX-TA-AmB group. Additionally, Rhodamine B (RhB) was encapsulated as a fluorescent marker in all formulations, and fluorescence imaging of the head region of the rabbits was conducted using IVIS (excitation/emission: 530/600 nm) at 0 and 30 s and at 3, 10, 20, 45, and 90 min post-administration. Images were processed using ImageJ software (National Institutes of Health, USA).

For in vitro IVIS experiments, freshly excised porcine corneas from a local abattoir were used. Each cornea was fixed to a 12-well plate. The plates were maintained at 37 °C on a metal heating plate. After administering 50 μL of PX or PX-TA-AmB to each cornea, PBS was used to wash each cornea at a flow rate of 10 mL/min. After 30 min, fluorescence imaging was performed using IVIS (excitation/emission: 530/600 nm).

For drug tracing experiments in corneas, PX-TA-AmB was additionally loaded with Cy3 (0.5 mg/mL) using the thin-film hydration method, while the AmB group was mixed with Cy3 at the same concentration. Mouse corneal epithelia were debrided using an epithelial scraper, followed by administration of 5 μL of different formulations. At predetermined time points, mice were euthanized, and the excised eyeballs were rapidly processed for frozen sectioning and observed under SP8 laser scanning confocal microscopy (Leica, Wetzlar, Germany) (excitation/emission: 550/570 nm).

4.9. In vitro antifungal activity assays

The *Candida albicans* strain (CA, ATCC MYA-2876) was purchased from the China General Microbiological Culture Collection Center.

To evaluate the in vitro antifungal activity of PX-TA-AmB, frozen CA strains were initially inoculated onto Sabouraud dextrose agar (SDA) plates to isolate single colonies. The isolated single colony was inoculated into Sabouraud dextrose broth (SDB) and cultured at 30 °C for 24 h. Then, 1 mL of fungal suspension (1×10^6 CFU/mL) was treated with 1 μL of either PBS (control), AmB (0.2 % suspension), PX-TA (18 % P407, 5 % P188, 2.5 % TA), or PX-TA-AmB (18 % P407, 5 % P188, 2.5 % TA, 0.2 % AmB); these represented the different treatment groups. The mixtures were incubated at 30 °C for 24 h. Following incubation, 100 μL of each suspension was transferred to a 96-well plate, and cell growth was assessed by measuring the OD_{600}. Subsequently, 10 μL of each culture was plated onto SDA plates and incubated at 30 °C for 24 h. Colony-forming units (CFUs) were counted to determine viable cell numbers. For the fungal disk diffusion assay, sterile filter paper disks (6 mm diameter) were soaked in AmB, PX-TA, or PX-TA-AmB solutions for 1 min. Then, 10 μL of the fungal suspension (1×10^7 CFU/mL) was spread onto SDA plates, and the soaked disks were placed onto the agar surface. After incubation at 30 °C for 24 h, the diameters of the inhibition zones were measured. Images were processed using ImageJ software.

For SEM imaging of fungal morphology, fungal suspensions treated with the aforementioned therapeutic regimens were centrifuged at 4000 rpm and washed with PBS. The specimens were then fixed in 4 % glutaraldehyde solution at 4 °C for 12 h, followed by sequential dehydration, drying out, and conductive coating. SEM images were acquired using a Hitachi Regulus 8100 SEM (Hitachi, Tokyo, Japan).

For antibiofilm assessment, fungal suspensions (1 mL, 1×10^7 CFU/mL) were cultured in 24-well plates at 30 °C for 12 h, followed by treatment with the previously described therapeutic regimens for 48 h. Different staining protocols were employed for distinct analytical purposes. For crystal violet staining, samples were gently washed with PBS and stained with 200 μL of 0.2 % crystal violet solution, followed by PBS washing and photography. For fluorescence imaging, samples were stained using the LIVE/DEAD Biofilm Viability kit (Thermo Fisher Scientific, Waltham, MA, USA) according to the manufacturer's protocol. Three-dimensional imaging was performed using SP8 laser scanning confocal microscopy (Leica, Wetzlar, Germany).

4.10. Animal experiments

Female C57BL/6 mice (6–8 weeks old) free of specific pathogens were purchased from Vital River (Beijing, China), and healthy female New Zealand white rabbits (2.0–2.5 kg) were purchased from Tianjin Yuda (Tianjin, China). The experiment was approved by the Ethics Committee of the Institute of Radiation Medicine, Chinese Academy of Medical Sciences (approval number: IRM/2-IACUC-2409-038) and was conducted in accordance with the ARVO Statement for the Use of Animals in Ophthalmic and Vision Research.

4.11. In vivo treatment efficacy and visual function assessment

All mouse FK models were established by inoculating *Candida albicans* into scarified corneas. Briefly, the mice were anesthetized via intraperitoneal injection of tribromoethanol (200 mg/kg), and a 30G needle was used to create 30 crosshatch scratches on the right cornea of each mouse to induce corneal scarring. Subsequently, 5 μL of a *Candida albicans* suspension (1×10^6/mL) was evenly distributed on the corneal surface as an inoculum. After 24 h of inoculation, the established FK mice were randomly divided into four groups and treated according to the following regimens: the control group (5 μL of PBS administered once daily); the AmB group (5 μL of 0.20 % AmB suspension administered six times daily to simulate the first-line clinical treatment); the PX-TA group (5 μL of PX-TA eye drops administered once daily); and the PX-TA-AmB group (5 μL of PX-TA-AmB eye drops administered once daily). Additionally, a natamycin group (5 μL of 0.20 % natamycin suspension administered six times daily) was preliminarily compared with the AmB group through anterior segment photography, fluorescein sodium staining, and histological evaluation, and was excluded due to inferior therapeutic efficacy.

Anterior segment images of all mice were captured every two days using a slit lamp microscope (Topcon Healthcare, SL-D701, China), and fluorescein sodium-stained images of the ocular surface were collected under cobalt blue light at the designated time points. Signs of inflammatory changes in the anterior segment were observed every two days, and their severity were scored and recorded based on established criteria [56](Table S3). On day 4 posttreatment, a subset of the mice was euthanized, and their eyeballs were harvested for fungal burden experiments and histopathological examinations related to fungal viability. On day 6 posttreatment, the eyeballs were collected for cytokine assays and etiological histopathological analyses.

Visual function assessment was performed on day 10 post-treatment and included evaluations of both visual electrophysiology and animal ethology. Visual function was assessed using a visual electrophysiology system (Roland consult, Germany) according to the electrode mounting method described in the ISCEV standards to record full-field ERG patterns. Additionally, light aversion behavior was evaluated using a light–dark box (Zhongshi Technology, China); here, the mice were placed in a closed box divided into bright and dark areas, and their activity time and choice behavior under different lighting conditions were recorded using infrared photography. Images were processed using ImageJ software.

4.12. Transcriptomic analysis

Corneal samples collected from FK (control, $n = 3$) and PX-TA-AmB-treated ($n = 3$) mice were immediately preserved in liquid nitrogen. The harvested tissues were subjected to paired-end sequencing (PE150) using an Illumina NovaSeq 6000 platform (Illumina Inc., San Diego, CA, USA) at LC Biotechnology Co., Ltd. (Hangzhou, China), following the manufacturer-recommended protocols.

4.13. In vivo corneal wound healing evaluation

All New Zealand White rabbits were anesthetized before surgery with intravenous sodium pentobarbital (50 mg/kg) for general anesthesia and 0.5 % proparacaine hydrochloride eye drops for topical anesthesia. A 3.5 mm diameter and 1/3 corneal thickness epithelial and stromal defect was created at the center of the right cornea of each rabbit using a corneal trephine. The established corneal injury model was randomly divided into the following four groups: the control group (20 μL of PBS, once daily), the PX group (20 μL of PX eye drops, once daily), the PX-TA group (20 μL of PX-TA eye drops, once daily), and the PX-TA-AmB group (20 μL of PX-TA-AmB eye drops, once daily). Anterior segment photography and fluorescein sodium staining were performed at predetermined time points. After 28 days, the rabbits were euthanized, and the eyeballs were harvested for further pathological examination. Images were processed using ImageJ software.

4.14. In vivo pharmacokinetics assay

The established corneal injury New Zealand White rabbit model was randomly divided into two groups ($n = 3$): AmB group (20 μL 0.20 % AmB suspension) and PX-TA-AmB group (20 μL PX-TA-AmB eye drops). At predetermined time intervals, 70 μL aqueous humor were collected and mixed with 400 μL methanol, and centrifuged at 12000 rpm for 10 min and analyzed by HPLC. Meanwhile, the corneas of rabbits were harvested, weighed and homogenized by glass homogenizer. The homogenates were extracted by 500 μL 75 % methanol, and centrifuged at 12000 rpm for 10 min. Then the supernatants were collected and evaporated at 30 °C using Eppendorf Concentrator plus (Eppendorf Co., GER). The residue was redissolved in 200 μL methanol and analyzed by HPLC.

4.15. ICP-MS analysis of corneal copper concentration

Fresh rabbit corneal tissues were weighed after excess surface moisture was removed using filter paper. The tissues were then mixed with HNO_3 and subjected to digestion in a high-pressure microwave digestion system. Subsequently, the samples were diluted and brought to a final volume of 10 mL. Quantitative analysis of copper concentration was performed using inductively coupled plasma mass spectrometry (ICP-MS, Agilent 7800, CA, USA), with concurrent blank controls and standard curve calibration.

4.16. LOX relative activity assay

A semi-quantitative activity assay was performed using a LOX Activity Assay Kit (Abcam, Cambridge, UK). Corneal tissues were homogenized in 0.5 mL extraction buffer (containing 6 M urea, 10 mM Tris, and protease inhibitors), followed by centrifugation at 12000 rpm for 10 min at 4 °C. The supernatant was collected, appropriately diluted with PBS, and 50 μL was added to each microplate well. 50 μL of LOX Reaction Mix was added to each well to make the total assay volume 100 μL. The fluorescence at 535/590 nm was measured after incubation at 37 °C for 30 min.

4.17. Pathological histology

The harvested eyeballs were immediately fixed in 4 % paraformaldehyde and left at 4 °C for 24 h. After gradient dehydration, the tissues were embedded in paraffin, and 4 μm paraffin sections were prepared for further staining. The sections were subjected to hematoxylin and eosin (H&E) staining, periodic acid-Schiff (PAS) staining, Masson's trichrome staining, and Calcofluor white (CFW) staining. Images were captured using a light microscope (Olympus CX41, Tokyo, Japan). The corneal thickness in the H&E images was analyzed using ImageJ software.

4.18. Luminex analysis

Corneal tissues harvested on day 6 post-treatment from differently treated mice were homogenized, and proteins were extracted using RIPA buffer. Protein samples (45 μg) were sequentially incubated with microbeads (1 h), detection antibodies (30 min), and streptavidin-PE (10 min); afterward, the expression levels were measured using a Luminex 200 System (Luminex Corporation, Austin, TX, USA) with a Bio-Plex Pro Mouse 23-plex Kit (Bio-Rad, CA, USA).

4.19. Immunofluorescence staining

Eight-micron-thick frozen sections of eyeballs were prepared after fixation. Following permeabilization with 0.1 % Triton X-100 and blocking with 1 % BSA, the sections were incubated overnight at 4 °C with primary antibodies. The primary antibodies used included Ly6g (eBioscience, 14–5931, 1:50), CD86 (Proteintech, 13395-1-AP, 1:150), CD206 (Proteintech, 18704-1-AP, 1:150), MMP9 (Affinity Biosciences, AF5228, 1:200), α-SMA (Proteintech, 14395-1-AP, 1:150), IL-6 (Affinity Biosciences, DF6087, 1:200), and IL-1β (Affinity Biosciences, AF5103, 1:200). After being washed with PBS three times, the sections were incubated in the dark at room temperature for 1 h with either a goat anti-rat IgG secondary antibody (Jackson ImmunoResearch, 112-546-003, 1:500) or a goat anti-rabbit IgG secondary antibody (Jackson ImmunoResearch, 111-546-003, 1:500). Following another wash, the sections were mounted with an anti-fade reagent containing 4′,6-diamidino-2-phenylindole (DAPI) (Abbkine Scientific, Wuhan, China). Images were captured using SP8 laser scanning confocal microscopy. Images were processed using ImageJ software.

4.20. Western blot

On Day 6 posttreatment, the corneas from the mice were dissolved in 200 μL of RIPA buffer (Solarbio, China), followed by tissue homogenization, sonication, and centrifugation at 12,000 rpm for 15 min to collect the supernatant, and the protein concentration was measured using a BCA assay kit (Thermo Fisher Scientific, USA). The total protein was separated using sodium dodecyl sulfate polyacrylamide gel electrophoresis (SDS-PAGE) and transferred onto a 0.45 μm pore size polyvinylidene fluoride (PVDF) membrane (Millipore, Germany); this membrane was then blocked with 5 % milk at room temperature and incubated with primary antibodies overnight at 4 °C; these antibodies included p-PI3K (Cell Signaling Technology, 4228, 1:1000), PI3K (Cell Signaling Technology, 4257, 1:1000), p-Akt (ABclonal, AP1453, 1:1000), Akt (ABclonal, A18675, 1:2000), MAPK6 (Abcam, ab53277, 1:1000), IL-1β (Abcam, ab9722, 1:1000), MMP9 (Proteintech, 10375-2-AP, 1:1000), Vinculin (Proteintech, 26520-1-AP, 1:10000) and β-Actin (ABclonal, AC026, 1:20000). After three washes, the PVDF membrane was incubated with a goat anti-rabbit secondary antibody (Proteintech, SA00001-2, 1:10000) at room temperature for 1 h, and the protein bands were finally detected using enhanced chemiluminescence (ECL) (Thermo Fisher Scientific, USA). The bands were quantified via ImageJ software.

4.21. Real-time polymerase chain reaction (RT–PCR)

Real-time PCR (RT–PCR) was performed using the Universal RNA Purification Kit (EZBioscience, Roseville, USA) for the extraction of the total RNA from corneas, followed by reverse transcription of RNA samples using the TransScript All-in-One First-Strand cDNA Synthesis SuperMix for qPCR Kit (Transgen, China). qPCR was then conducted using a LightCycler 96 system (Roche, Mannheim, Germany). The data were analyzed using the $2^{-\Delta\Delta Ct}$ method, and all primers were purchased from Sangon Biotech (Shanghai, China). The sequences of the primers are listed in Table S4.

4.22. Biosafety assessment experiments

HCECs and HCSCs were provided by Professor Yan Wang from Tianjin Eye Hospital and used to assess the cytotoxicity of PX-TA-AmB using the Calcein/PI Cell Viability Assay Kit (Beyotime, China). Briefly, HCECs and HCSCs (1×10^6 cells/mL) were seeded into 6-well plates at 1 mL per well and incubated at 37 °C in a 5 % CO_2 atmosphere. The cells were treated with 1 μL of either PBS (control), AmB (0.2 % suspension), PX-TA (18 % P407, 5 % P188, 2.5 % TA), or PX-TA-AmB (18 % P407, 5 % P188, 2.5 % TA, 0.2 % AmB) for 24 h. Following the manufacturer's instructions, the cells were stained with calcein-AM and propidium iodide (PI) dyes. Live and dead cells were visualized under a fluorescence microscope and appeared green and red, respectively.

The ocular irritation potential of PX-TA-AmB was evaluated via the HET-CAM assay. Specific pathogen-free (SPF)-grade fertilized chicken eggs (Zhushun Biotechnology, China) were incubated at 38 ± 0.5 °C. On the 10th day of incubation, the eggs were illuminated to locate the air cell, and a 2×2 cm^2 section of the eggshell was carefully removed using forceps. After the inner membrane was moistened with 0.5 mL of saline, the membrane was gently peeled off. Subsequently, 0.3 mL of the test formulations (AmB or PX-TA-AmB) was applied to the CAM. The control solutions consisted of 0.9 % (w/v) NaCl as a negative control, and 0.1 M NaOH and 1 % (w/v) SDS served as positive controls to induce hemorrhage and vasoconstriction, respectively. Changes in the CAM were observed and recorded within 5 min. ISs were calculated using the following formula:

$IS = [5 \times (301 - \text{time to hemorrhage (s)}/300)] + [7 \times (301 - \text{time to vasoconstriction (s)}/300)] + [9 \times (301 - \text{time to coagulation (s)}/300)]$

Ocular irritation was classified as follows: $IS < 1$, no irritation; $1 \leq IS < 5$, mild irritation; $5 \leq IS < 9$, moderate irritation; and $IS \geq 9$, severe irritation.

In vivo, PX-TA-AmB or PBS was administered to the right conjunctival sac of each mouse once daily. On day 10, the corneas were stained with 2 μL of 0.5 % sodium fluorescein for observation. Subsequently, mouse corneas (day 10 and day 28) and main visceral organs (day 10) were harvested for histological evaluation. Additionally, mouse intraocular pressure (IOP) in different groups was measured using an TONOLAB tonometer (iCare, Finland) throughout the 28-day continuous administration period to monitor the formulation's effect on IOP.

4.23. Statistical analysis

All data were analyzed using GraphPad Prism 8 software (GraphPad Software, CA, USA). Experimental results are presented as means ± standard deviation from at least three independent biological replicates. Assumptions of normality and homogeneity of variances were verified prior to conducting ANOVA. Statistical comparisons were made using one-way ANOVA with Tukey's test for multiple comparisons and two-way ANOVA with the Sidak test for multiple comparisons. Differences were considered significant at P values less than 0.05.

CRediT authorship contribution statement

Maoyu Cai: Writing – review & editing, Writing – original draft, Visualization, Validation, Software, Methodology, Investigation, Data curation, Conceptualization. **Haiping Zhong:** Writing – review & editing, Validation, Methodology, Investigation, Formal analysis, Data curation. **Xindi Wang:** Writing – review & editing, Software, Methodology, Conceptualization. **Liangpin Li:** Writing – review & editing, Validation. **Xueyan Zhou:** Writing – review & editing, Methodology. **Yan Wang:** Writing – review & editing, Methodology, Funding acquisition, Conceptualization. **Xia Hua:** Writing – review & editing, Investigation, Funding acquisition. **Shutao Guo:** Writing – review & editing, Writing – original draft, Investigation, Funding acquisition, Conceptualization. **Xiaoyong Yuan:** Writing – review & editing, Writing – original draft, Methodology, Investigation, Conceptualization.

Availability of data

The data will be made available upon reasonable request.

Ethics approval and consent to participate

The experiment was approved by the Ethics Committee of the Institute of Radiation Medicine, Chinese Academy of Medical Sciences (approval number: IRM/2-IACUC-2409-038) and was conducted in accordance with the ARVO Statement for the Use of Animals in Ophthalmic and Vision Research.

Declaration of competing interest

The authors declare the following personal relationships which may be considered as potential competing interests: Xia Hua is currently employed by Aier Eye Institute.

Acknowledgments

This work was supported by the National Natural Science Foundation of China (Nos. 82371033, 82471053, 32171386, 32201157, and U23A20488), the Beijing-Tianjin-Hebei Basic Research Cooperation Project (No. 22JCZXJC00030), the Tianjin Key Medical Discipline (Specialty) Construction Project (TJYXZDXK-016A), the Tianjin Municipal Science and Technology Program (22JCZDJC00260), and the Nankai University Eye Institute (Nos. NKYKD202304 and NKYKK202207).

Appendix A. Supplementary data

Supplementary data to this article can be found online at https://doi.org/10.1016/j.bioactmat.2025.04.011.

References

[1] L. Brown, A.K. Leck, M. Gichangi, M.J. Burton, D.W. Denning, The global incidence and diagnosis of fungal keratitis, Lancet Infect. Dis. 21 (2021) e49–e57, https://doi.org/10.1016/s1473-3099(20)30448-5.

[2] A.C. Bisen, S.N. Sanap, S. Agrawal, A. Biswas, A. Mishra, S.K. Verma, V. Singh, R. S. Bhatta, Etiopathology, epidemiology, diagnosis, and treatment of fungal keratitis, ACS Infect. Dis. 10 (2024) 2356–2380, https://doi.org/10.1021/acsinfecdis.4c00203.

[3] P. Lalitha, N.V. Prajna, A. Kabra, K. Mahadevan, M. Srinivasan, Risk factors for treatment outcome in fungal keratitis, Ophthalmology 113 (2006) 526–530, https://doi.org/10.1016/j.ophtha.2005.10.063.

[4] V. Agrawal, J. Biswas, H.N. Madhavan, G. Mangat, M.K. Reddy, J.S. Saini, S. Sharma, M. Srinivasan, Current perspectives in infectious keratitis, Indian J. Ophthalmol. 42 (1994) 171–192.

[5] C. García-López, M. Rodríguez-Calvo-de-Mora, D. Borroni, J.M. Sánchez-González, V. Romano, C. Rocha-de-Lossada, The role of matrix metalloproteinases in infectious corneal ulcers, Surv. Ophthalmol. 68 (2023) 929–939, https://doi.org/10.1016/j.survophthal.2023.06.007.

[6] S. Kaur, P. Sohnen, S. Swamynathan, Y. Du, E.M. Espana, S.K. Swamynathan, Molecular nature of ocular surface barrier function, diseases that affect it, and its relevance for ocular drug delivery, Ocul. Surf. 30 (2023) 3–13, https://doi.org/10.1016/j.jtos.2023.08.001.

[7] A. Austin, T. Lietman, J. Rose-Nussbaumer, Update on the management of infectious keratitis, Ophthalmology 124 (2017) 1678–1689, https://doi.org/10.1016/j.ophtha.2017.05.012.

[8] N.V. Prajna, M. Srinivasan, P. Lalitha, T. Krishnan, R. Rajaraman, M. Ravindran, J. Mascarenhas, C.E. Oldenburg, K.J. Ray, S.D. McLeod, N.R. Acharya, T. M. Lietman, Differences in clinical outcomes in keratitis due to fungus and bacteria, JAMA Ophthalmol 131 (2013) 1088–1089, https://doi.org/10.1001/jamaophthalmol.2013.1612.

[9] Y. Yang, A. Lockwood, Topical ocular drug delivery systems: innovations for an unmet need, Exp. Eye Res. 218 (2022) 109006, https://doi.org/10.1016/j.exer.2022.109006.

[10] D. Shi, X. Qi, L. Ma, L. Zhao, S. Dou, Y. Wang, Q. Zhou, Y. Zhang, C. Yang, H. Wang, L. Xie, Fabrication of nanozyme-thixotropic anionic hydrogel coating with multi-enzyme-mimicking activity for the treatment of fungal keratitis, Chem. Eng. J. 486 (2024) 150264, https://doi.org/10.1016/j.cej.2024.150264.

[11] L. Dong, Z. Fan, B. Fang, X. Zhao, H. Yao, G. Cai, S. Yang, G. Zhang, X. Cheng, Y. Feng, S. Mi, W. Sun, Oriented cellulose hydrogel: directed tissue regeneration for reducing corneal leukoplakia and managing fungal corneal ulcers, Bioact. Mater. 41 (2024) 15–29, https://doi.org/10.1016/j.bioactmat.2024.07.008.

[12] R. Sun, J. Zhang, X. Chen, Y. Deng, J. Gou, T. Yin, H. He, X. Tang, X. Ni, L. Yang, Y. Zhang, An adaptive drug-releasing contact lens for personalized treatment of ocular infections and injuries, J. Contr. Release 369 (2024) 114–127, https://doi.org/10.1016/j.jconrel.2024.03.040.

[13] X. Wang, I.S. Mohammad, L. Fan, Z. Zhao, M. Nurunnabi, M.A. Sallam, J. Wu, Z. Chen, L. Yin, W. He, Delivery strategies of amphotericin B for invasive fungal infections, Acta Pharm. Sin. B 11 (2021) 2585–2604, https://doi.org/10.1016/j.apsb.2021.04.010.

[14] H. Han, S. Li, M. Xu, Y. Zhong, W. Fan, J. Xu, T. Zhou, J. Ji, J. Ye, K. Yao, Polymer- and lipid-based nanocarriers for ocular drug delivery: current status and future perspectives, Adv. Drug Deliv. Rev. 196 (2023) 114770, https://doi.org/10.1016/j.addr.2023.114770.

[15] S. Ahmed, M.M. Amin, S. Sayed, Ocular drug delivery: a comprehensive review, AAPS PharmSciTech 24 (2023) 66, https://doi.org/10.1208/s12249-023-02516-9.

[16] B. Ahmed, S. Jaiswal, S. Naryal, R.M. Shah, R.G. Alany, I.P. Kaur, In situ gelling systems for ocular drug delivery, J. Contr. Release 371 (2024) 67–84, https://doi.org/10.1016/j.jconrel.2024.05.031.

[17] S. Ghosh, Y.-H. Su, C.-J. Yang, J.-Y. Lai, Design of highly adhesive urchin-like gold nanostructures for effective topical drug administration and symptomatic relief of corneal dryness, Small Struct 6 (2025) 2400484, https://doi.org/10.1002/sstr.202400484.

[18] T.Y. Ger, C.J. Yang, H.L. Bui, S.J. Lue, C.H. Yao, J.Y. Lai, Alginate-functionalized nanoceria as ion-responsive eye drop formulation to treat corneal abrasion, Carbohydr. Polym. 352 (2025) 123164, https://doi.org/10.1016/j.carbpol.2024.123164.

[19] C.J. Yang, A. Anand, C.C. Huang, J.Y. Lai, Unveiling the power of gabapentin-loaded nanoceria with multiple therapeutic capabilities for the treatment of dry eye disease, ACS Nano 17 (2023) 25118–25135, https://doi.org/10.1021/acsnano.3c07817.

[20] C.J. Yang, D.D. Nguyen, J.Y. Lai, Poly(l-Histidine)-Mediated on-demand therapeutic delivery of roughened ceria nanocages for treatment of chemical eye injury, Adv. Sci. 10 (2023) e2302174, https://doi.org/10.1002/advs.202302174.

[21] H. Shi, J. Zhou, Y. Wang, Y. Zhu, D. Lin, L. Lei, S. Vakal, J. Wang, X. Li, A rapid corneal healing microneedle for efficient ocular drug delivery, Small 18 (2022) e2104657, https://doi.org/10.1002/smll.202104657.

[22] K. Huang, R. Guo, H. Luo, H. Liu, D. Chen, T. Deng, J. Li, J. He, Z. Xu, M. Li, Q. He, Mucoadhesive liposomal delivery system synergizing anti-inflammation and anti-oxidation for enhanced treatment against dry eye disease, J. Contr. Release 368 (2024) 318–328, https://doi.org/10.1016/j.jconrel.2024.02.043.

[23] H.L. Bui, Y.H. Su, C.J. Yang, C.J. Huang, J.Y. Lai, Mucoadhesive, antioxidant, and lubricant catechol-functionalized poly(phosphobetaine) as biomaterial nanotherapeutics for treating ocular dryness, J. Nanobiotechnol. 22 (2024) 160, https://doi.org/10.1186/s12951-024-02448-x.

[24] P.H. Lin, H.J. Jian, Y.J. Li, Y.F. Huang, A. Anand, C.C. Huang, H.J. Lin, J.Y. Lai, Alleviation of dry eye syndrome with one dose of antioxidant, anti-inflammatory, and mucoadhesive lysine-carbonized nanogels, Acta Biomater. 141 (2022) 140–150, https://doi.org/10.1016/j.actbio.2022.01.044.

[25] Y. Yu, Y. Cheng, J. Tong, L. Zhang, Y. Wei, M. Tian, Recent advances in thermo-sensitive hydrogels for drug delivery, J. Mater. Chem. B 9 (2021) 2979–2992, https://doi.org/10.1039/d0tb02877k.

[26] Y.C. Kim, M.D. Shin, S.F. Hackett, H.T. Hsueh, E.S.R. Lima, A. Date, H. Han, B. J. Kim, A. Xiao, Y. Kim, L. Ogunnaike, N.M. Anders, A. Hemingway, P. He, A. S. Jun, P.J. McDonnell, C. Eberhart, I. Pitha, D.J. Zack, P.A. Campochiaro, J. Hanes, L.M. Ensign, Gelling hypotonic polymer solution for extended topical drug delivery to the eye, Nat. Biomed. Eng. 4 (2020) 1053–1062, https://doi.org/10.1038/s41551-020-00606-8.

[27] R.L. Shapiro, K.M. Bockley, H.T. Hsueh, M.B. Appell, D.M. Carter, J. Ortiz, C. Brayton, L.M. Ensign, Hypotonic, gel-forming delivery system for vaginal drug administration, J. Contr. Release 371 (2024) 101–110, https://doi.org/10.1016/j.jconrel.2024.05.037.

[28] S. Wang, W.-Y. Wu, J.C.C. Yeo, X.Y.D. Soo, W. Thitsartarn, S. Liu, B.H. Tan, A. Suwardi, Z. Li, Q. Zhu, X.J. Loh, Responsive hydrogel dressings for intelligent wound management, BMEMat 1 (2023) e12021, https://doi.org/10.1002/bmm2.12021.

[29] Q. Wang, X. Zhao, F. Yu, P.H. Fang, L. Liu, X. Du, W. Li, D. He, Y. Bai, S. Li, J. Yuan, Photocurable and temperature-sensitive bioadhesive hydrogels for sutureless sealing of full-thickness corneal wounds, Small Methods 8 (2024) e2300996, https://doi.org/10.1002/smtd.202300996.

[30] D.D. Nguyen, L.J. Luo, J.Y. Lai, Dendritic effects of injectable biodegradable thermogels on pharmacotherapy of inflammatory glaucoma-associated degradation of extracellular matrix, Adv. Healthcare Mater. 8 (2019) e1900702, https://doi.org/10.1002/adhm.201900702.

[31] L.J. Luo, D.D. Nguyen, J.Y. Lai, Benzoic acid derivative-modified chitosan-g-poly (N-isopropylacrylamide): methoxylation effects and pharmacological treatments of Glaucoma-related neurodegeneration, J. Contr. Release 317 (2020) 246–258, https://doi.org/10.1016/j.jconrel.2019.11.038.

[32] E. Giuliano, D. Paolino, M. Fresta, D. Cosco, Mucosal applications of poloxamer 407-based hydrogels: an overview, Pharmaceutics 10 (2018) 159, https://doi.org/10.3390/pharmaceutics10030159.

[33] S. Li, Z. Lu, Y. Huang, Y. Wang, Q. Jin, X. Shentu, J. Ye, J. Ji, K. Yao, H. Han, Anti-oxidative and anti-inflammatory micelles: break the dry eye vicious cycle, Adv. Sci. 9 (2022) e2200435, https://doi.org/10.1002/advs.202200435.

[34] J. Huang, T. Jiang, J. Qie, X. Cheng, Y. Wang, Y. Ye, Z. Yang, H. Yan, K. Yao, H. Han, Biologically inspired bioactive hydrogels for scarless corneal repair, Sci. Adv. 10 (2024) eadt1643, https://doi.org/10.1126/sciadv.adt1643.

[35] M. Shin, H.A. Lee, M. Lee, Y. Shin, J.J. Song, S.W. Kang, D.H. Nam, E.J. Jeon, M. Cho, M. Do, S. Park, M.S. Lee, J.H. Jang, S.W. Cho, K.S. Kim, H. Lee, Targeting protein and peptide therapeutics to the heart via tannic acid modification, Nat. Biomed. Eng. 2 (2018) 304–317, https://doi.org/10.1038/s41551-018-0227-9.

[36] J. Mu, Y. Du, X. Li, R. Yan, H. Zhong, M. Cai, N. Yu, J. Zhang, X. Yuan, X. Hua, S. Guo, Collagen-anchored cascade nanoreactors with prolonged intratumoral retention for combined cancer starvation and chemotherapy, Chem. Eng. J. 451 (2023) 138554, https://doi.org/10.1016/j.cej.2022.138554.

[37] M. Pan, Z. Ren, X. Ma, L. Chen, G. Lv, X. Liu, S. Li, X. Li, J. Wang, A biomimetic peptide-drug supramolecular hydrogel as eyedrops enables controlled release of ophthalmic drugs, Acta Biomater. 167 (2023) 195–204, https://doi.org/10.1016/j.actbio.2023.06.036.

[38] X. Sha, L. Chan, X. Fan, P. Guo, T. Chen, L. Liu, J. Zhong, Thermosensitive tri-block polymer nanoparticle-hydrogel composites as payloads of natamycin for antifungal therapy against Fusarium solani, Int. J. Nanomed. 17 (2022) 1463–1478, https://doi.org/10.2147/ijn.S332127.

[39] T. Zhou, S. Li, J. Zhu, G. Zeng, Z. Lv, M. Zhang, K. Yao, H. Han, Rosmarinic acid-grafted gelatin nanogels for efficient diquafosol delivery in dry eye disease therapy, J. Contr. Release 373 (2024) 306–318, https://doi.org/10.1016/j.jconrel.2024.07.026.

[40] T. Gratieri, G.M. Gelfuso, E.M. Rocha, V.H. Sarmento, O. de Freitas, R.F. Lopez, A poloxamer/chitosan in situ forming gel with prolonged retention time for ocular delivery, Eur. J. Pharm. Biopharm. 75 (2010) 186–193, https://doi.org/10.1016/j.ejpb.2010.02.011.

[41] J.Y. Lee, H.H. Shin, C. Cho, J.H. Ryu, Effect of tannic acid concentrations on temperature-sensitive sol-gel transition and stability of tannic acid/pluronic F127 composite hydrogels, Gels 10 (2024), https://doi.org/10.3390/gels10040256.

[42] N. Efron, G. Young, N.A. Brennan, Ocular surface temperature, Curr. Eye Res. 8 (1989) 901–906.

[43] L. Kessel, L. Johnson, H. Arvidsson, M. Larsen, The relationship between body and ambient temperature and corneal temperature, Investig. Ophthalmol. Vis. Sci. 51 (2010) 6593–6597, https://doi.org/10.1167/iovs.10-5659.

[44] I. Krtalić, S. Radošević, A. Hafner, M. Grassi, M. Nenadić, B. Cetina-Čižmek, J. Filipović-Grčić, I. Pepić, J. Lovrić, D-optimal design in the development of rheologically improved in situ forming ophthalmic gel, J. Pharmaceut. Sci. 107 (2018) 1562–1571, https://doi.org/10.1016/j.xphs.2018.01.019.

[45] L. Augis, C.H. Nguyễn, C. Ciseran, A. Wacha, F. Mercier-Nomé, S. Domenichini, C. Sizun, S. Fourmentin, F.-X. Legrand, Hydrophobic binary mixtures containing amphotericin B as lipophilic solutions for the treatment of cutaneous leishmaniasis, Int. J. Pharm. 662 (2024) 124486, https://doi.org/10.1016/j.ijpharm.2024.124486.

[46] M.E. Klepser, E.J. Wolfe, R.N. Jones, C.H. Nightingale, M.A. Pfaller, Antifungal pharmacodynamic characteristics of fluconazole and amphotericin B tested against Candida albicans, Antimicrob. Agents Chemother. 41 (1997) 1392–1395, https://doi.org/10.1128/aac.41.6.1392.

[47] T. Jia, F. Stapleton, F. Iqbal, J. Showyin, D. Roy, M. Roy, J. Tan, Comparison of eye drop retention time using fluorophotometry in three commercially available lubricant eye drops, Optom. Vis. Sci. 101 (2024) 603–607, https://doi.org/10.1097/opx.0000000000002172.

[48] R.R. Reddy, B.V. Phani Kumar, G. Shanmugam, B. Madhan, A.B. Mandal, Molecular level insights on collagen-polyphenols interaction using spin-relaxation and saturation transfer difference NMR, J. Phys. Chem. B 119 (2015) 14076–14085, https://doi.org/10.1021/acs.jpcb.5b07911.

[49] E. Thiels, E.K. Hoffman, M.B. Gorin, A reliable behavioral assay for the assessment of sustained photophobia in mice, Curr. Eye Res. 33 (2008) 483–491, https://doi.org/10.1080/02713680802130347.

[50] R.C. de Oliveira, S.E. Wilson, Fibrocytes, wound healing, and corneal fibrosis, Investig. Ophthalmol. Vis. Sci. 61 (2020) 28, https://doi.org/10.1167/iovs.61.2.28.

[51] S. Luan, X. Peng, J. Lin, Y. Zhang, L. Zhan, J. Yin, J. Luan, X. Ji, G. Zhao, Gallic acid ameliorates Aspergillus fumigatus keratitis through reducing fungal load and suppressing the inflammatory response, Investig. Ophthalmol. Vis. Sci. 63 (2022) 12, https://doi.org/10.1167/iovs.63.12.12.

[52] X. Ji, X. Peng, X. Long, Y. Zhang, J. Lin, J. Yin, R. Zhang, G. Zhao, Laccase-mediated functionalization of natamycin by gallic acids for the therapeutic effect on Aspergillus fumigatus keratitis, Eur. J. Pharmacol. 926 (2022) 175041, https://doi.org/10.1016/j.ejphar.2022.175041.

[53] Q. Cai, W. Zhou, W. Wang, B. Dong, D. Han, T. Shen, C.J. Creighton, D.D. Moore, F. Yang, MAPK6-AKT signaling promotes tumor growth and resistance to mTOR kinase blockade, Sci. Adv. 7 (2021) eabi6439, https://doi.org/10.1126/sciadv.abi6439.

[54] Y. Xu, F. Cai, Y. Zhou, J. Tang, J. Mao, W. Wang, Z. Li, L. Zhou, Y. Feng, K. Xi, Y. Gu, L. Chen, Magnetically attracting hydrogel reshapes iron metabolism for tissue repair, Sci. Adv. 10 (2024) eado7249, https://doi.org/10.1126/sciadv.ado7249.

[55] W. Chen, A. Yang, J. Jia, Y.V. Popov, D. Schuppan, H. You, Lysyl oxidase (LOX) family members: rationale and their potential as therapeutic targets for liver fibrosis, Hepatology 72 (2020) 729–741, https://doi.org/10.1002/hep.31236.

[56] T.G. Wu, K.R. Wilhelmus, B.M. Mitchell, Experimental keratomycosis in a mouse model, Investig. Ophthalmol. Vis. Sci. 44 (2003) 210–216, https://doi.org/10.1167/iovs.02-0446.